MAX-DOAS observations of formaldehyde and nitrogen dioxide at three sites in Asia and comparison with the global chemistry transport model CHASER

Hossain Mohamed Syedul Hoque[1], Kengo Sudo[1,2], Hitoshi Irie[3], Alessandro Damiani[3], Manish Naja[4], and Al Mashroor Fatmi[3]

[1]Graduate School of Environmental Studies, Nagoya University, Nagoya, 4640064, Japan

[2]Japan Agency for Marine-Earth Science and Technology (JAMSTEC), Kanagawa, 2370061, Japan

[3]Center for Environmental Remote Sensing (CEReS), Chiba University, Chiba,2638522, Japan

[4]Aryabhatta Research Institute for Observational Sciences (ARIES), Manora Peak, Nainital-263001, Uttarakhand, India

Correspondence to: Hossain Mohammed Syedul Hoque (hoque.hossain.mohammed.syedul.u6@f.mail.nagoya-u.ac.jp)

Abstract. Formaldehyde (HCHO) and nitrogen dioxide (NO_2) concentrations and profiles were retrieved from ground-based multi-axis differential optical absorption spectroscopy (MAX-DOAS) observations during January 2017 - December 2018 at three sites in Asia: (1) Phimai (15.18°N, 102.5°E), Thailand; (2) Pantnagar (29°N, 78.90°E) in the Indo Gangetic Plain (IGP), India; and (3) Chiba (35.62°N, 140.10°E), Japan. Retrievals were performed using the Japanese MAX-DOAS profile retrieval algorithm ver. 2 (JM2). The observations were used to evaluate the NO_2 and HCHO partial columns and profiles (0 - 4 km) simulated using the CHASER global chemistry transport model (CTM). At all three sites, the NO_2 and HCHO concentrations showed consistent seasonal variation throughout the investigated period. Biomass burning affected the HCHO and NO_2 variations at Phimai during the dry season and at Pantnagar during spring (March - May) and post-monsoon (September - November). Results found for the HCHO to NO_2 ratio (R_{FN}), an indicator of high ozone sensitivity, indicate that the transition region (i.e., $1< R_{FN} <2$) changes regionally, echoing the recent finding for R_{FN} effectiveness. Moreover, reasonable estimates of transition regions can be derived, accounting for the NO_2 - HCHO chemical feedback.

The model was also evaluated against global datasets of NO_2 and HCHO columns retrieved from Ozone Monitoring Instrument (OMI) observations. Despite underestimation, the model well simulated the satellite-observed global spatial distribution of NO_2 and HCHO, with respective spatial correlations (*r*) of 0.73 and 0.74, respectively. CHASER demonstrated good performance, reproducing the MAX-DOAS retrieved HCHO and NO_2 abundances at Phimai, mainly above 500 m from the surface. Model results agree with the measured variations within the one sigma standard deviation of the observations. Simulations at higher resolution improved the modeled NO_2 estimates for Chiba, reducing the mean bias error (MBE) for the 0 - 2 km height by 35%, but resolution-based improvements were limited to the surface layers. Sensitivity studies show that pyrogenic emissions at Phimai contribute to the HCHO and NO_2 concentrations, respectively up to 50 and 35%.

1 Introduction

Formaldehyde (HCHO), the most abundant carbonyl compound in the atmosphere, is a high-yield product of oxidization of all primary volatile organic compounds (VOCs) emitted from natural and anthropogenic sources by hydroxyl radicals (OH). Oxidation of long-lived VOCs such as methane produces a global HCHO background concentration of 0.2 – 1.0 ppbv in remote marine environments (Weller et al., 2000; Burkert et al., 2001; Singh et al., 2004; Sinreich et al., 2005). Aside from oxidation of VOCs, the significant sources of HCHO are direct emissions from biomass burning, industrial processes, fossil fuel combustion (Lee et al., 1997; Hak et al., 2005; Fu et al., 2008), and vegetation (Seco et al., 2007). However, oxidization of non-methane VOCs emitted from biogenic (e.g., isoprene) or anthropogenic (e.g., butene) sources govern the spatial variation of HCHO on a global scale (Franco et al., 2015). The sinks of HCHO include photolysis at wavelengths shorter than 400 nm, oxidation by OH, and wet deposition, thereby limiting the lifetime of HCHO to a few hours (Arlander et al., 1995).

Nitrogen dioxide (NO_2), an important atmospheric constituent, (1) participates in the catalytic formation of tropospheric ozone (O_3), (2) acts as a catalyst for stratospheric ozone (O_3) destruction (Crutzen, 1970), (3) contributes to the formation of aerosols (Jang and Kamens, 2001), (4) acts as a precursor of acid rain (Seinfeld and Pandis, 1998), and (5) strongly affects radiative forcing (Solomon et al. 1999; Lelieved et al., 2002;). Nitrogen oxides (NO_x = NO (nitric oxide) + NO_2) are emitted from natural and anthropogenic sources. Primary NO_x emission sources include biomass burning, fossil fuel

combustion, soil emissions, and lightning (Bond et al., 2001; Zhang et al., 2003). Not only do NO_x emissions degrade air quality; they are leading air pollutant (Ma et al., 2013). Both HCHO and NO_2 are important intermediates in the global VOC–HO_x (hydrogen oxides)–NO_x catalytic cycle, which governs O_3 chemistry in the troposphere (Lee et al., 1997; Houweling et al., 1998; Hak et al., 2005; Kanakidou et al., 2005). Thus, both trace gases play crucially important roles in tropospheric chemistry.

The observational sites examined for the present study have different atmospheric characteristics. Thailand is strongly affected by pollution because of rapid economic development and urbanization. Moreover, biomass burning in Southeast Asia is a significant source of O_3 precursors, contributing up to 30% of the total concentrations during the peak burning season (Amnuaylorajen et al., 2020; Khodmanee et al. 2021). Because of rapid industrialization, India the second most populous country in the world, is witnessing an increasing O_3 trend along with NO_2 and HCHO concentrations in all major cities (Mahajan et al; 2015; Lu et al, 2018;). The Indo-Gangetic Plain (IGP), which covers ~21% of the Indian subcontinent land area is hotspots of severe air pollution (Giles et al; 2005, Biswas et al; 2019). In contrast, surface O_3 concentrations have shown an increasing trend in Japan, despite decreasing NO_x and VOC concentrations related to emission control measures after 2000 (Irie et al., 2021). Therefore, observational and modeling studies must be conducted to improve our quantitative understanding of the O_3-NO_x-VOC relation in these regions.

Multi-axis differential optical absorption spectroscopy (MAX-DOAS), a well-established, unique, and powerful remote sensing method for measuring trace gases and aerosols, is based on the DOAS technique. Aerosols and trace gases are quantified using selective narrowband (high frequency) absorption features (Platt 1994; Platt and Stutz 2008). Spectral radiance measurements at different elevation angles (ELs) can provide profile information about atmospheric trace gases and aerosols (Hönninger et al., 2004; Wagner et al., 2004; Wittrock et al., 2004; Frieß et al., 2006; Irie et al., 2008a). Many studies have demonstrated the retrieval of aerosol and trace gas concentrations and profiles from MAX-DOAS observations, including NO_2 and HCHO (Clémer et al., 2010; Irie et al., 2011; Hendrick et al., 2014; Wang et al., 2014; Franco et al., 2015; Frieß et al., 2016).

The ability of MAX-DOAS to provide information related to surface concentrations, vertical profiles, and column densities makes it a good complement to ground-based in situ and satellite observations.

Moreover, the MAX-DOAS method uses narrowband absorption of the target compounds, thereby obviating any need for radiometric calibration of the instrument. Because of these advantages, MAX-DOAS systems are deployed for the assessment of aerosol and trace gases in regional and global observational networks such as BREDOM (Wittrock et al., 2004), BIRA-IASB (Clémer et al., 2010), and MADRAS (Kanaya et al., 2014). Such datasets are used, in but are not limited to, (1) air quality assessment and monitoring, (2) evaluation of chemistry-transport models (CTMS), and (3) validation of satellite data retrievals. Several studies have used MAX-DOAS datasets to validate tropospheric columns retrieved from satellite observations, including NO_2 and HCHO (Irie et al., 2008b; Ma et al., 2013; Chan et al., 2020; Ryan et al., 2020). However, limited MAX-DOAS datasets have been used to evaluate global CTMs. Vigouroux et al. (2009) and Franco et al. (2015) respectively used the MAX-DOAS HCHO datasets from Reunion Island and Jungfraujoch stations to evaluate the Intermediate Model of Annual and Global Evolution of Species (IMAGES) and GEOS-Chem model simulations. Kanaya et al. (2014) validated the Model for Interdisciplinary Research on Climate–Earth System Model – Chemistry (MIROC-ESM-CHEM) simulated NO_2 column densities with MAX-DOAS observations in Cape Hedo and Fukue in Japan. Kumar et al. (2021) used MAX-DOAS observations to evaluate the high-resolution regional model Meco(n)(MESSy-field ECHAM and COSMO model nested n times).

For this study, NO_2 and HCHO profiles retrieved from MAX-DOAS observations from the International air quality and sky research remote sensing (A-SKY) (http://atmos3.cr.chiba-u.jp/a-sky/) network sites are used to evaluate the global Chemical Atmospheric General Circulation Model for the Study of Atmospheric Environment and Radiative Forcing (CTM CHASER; Sudo et al., 2002). The three A-SKY sites of - (1) Phimai in Thailand (15.18°N, 102.56°E), (2) Pantnagar (29°N, 78.90°E) in the IGP in India, and (3) Chiba (35.62°N, 140.10°E) in Japan, are respectively representative of rural, semi-rural, and urban environments. CHASER has been used mostly for global-scale research (Sudo et al., 2007; Sekiya et al., 2014, 2018; Miyazaki et al., 2017). The study described herein is the first reported attempt to evaluate the CHASER-simulated NO_2 and HCHO profiles using MAX-DOAS observations in three different atmospheric environments. Moreover, few reports of the literature have described the use of MAX-DOAS datasets to evaluate global CTMs in South Asia and South-east Asia. Overall, this study was conducted

to provide important insights into model performances and to help reduce model uncertainties related to NO_2 and HCHO simulations in these regions.

The paper is structured in the following manner. First, the observation sites, MAX-DOAS instrumentation, and retrieval strategies are described in section 2. Section 2 also includes a short description of the CHASER model and Ozone Monitoring Instrument (OMI) HCHO and NO_2 retrievals. Next, the observations and the evaluation results are described in sections 3. Finally, the sensitivity study results are provided in section 3.4. and the concluding remarks in section 4.

2 Observations, datasets, and methods

2.1 Site Information

Continuous MAX-DOAS observations at Chiba, Phimai, and Pantnagar started respectively in 2012, 2014, and 2017. The measurements from January 2017 to December 2018 at all three sites are discussed herein. Phimai, a rural site, is located ~260 km north-east of the Bangkok metropolitan area and is unlikely to be affected by vehicular and industrial emissions. However, the site is affected by biomass burning during January - April. Two major air streams: the dry, cool north-east monsoon during November – mid-February and the wet, warm south-west monsoon during mid-May – September affect the climate in Phimai. As described by, Hoque et al. (2018), the climate classifications of Phimai are the (a) dry season (January – April), and (b) wet season (June – September).

Pantnagar, a semi-urban site in India, is located in the IGP. The Indian capital of New Delhi is situated at ~225 km south-west of the site. The low-altitude plains are on the south and west sides of the site. The Himalayan mountains are located to the north and east. An important roadway with moderate traffic volume and a small local airport lies within 3 km of the site. Rudrapur (~12 km south-west of Pantnagar) and Haldwani (~ 25 km north-east of Pantnagar) are the two major cities near Pantnagar, where industries (Fast moving Consumable Goods, electroplating, plywood, pharmaceuticals, automobile and allied industries (Banerjee and Srivastava 2009)) are located. The climate classification at Pantnagar is the

following: (1) winter (December–February), (2) spring (March-May), (3) summer monsoon (June–August), and (4) autumn (September–November).

Chiba, an urban site, is located ~40 km south-east of the Tokyo metropolitan region. Tokyo Bay, large-scale industries, and residential areas are located within a 50 km radius. Chiba has four distinct seasons: (1) spring (March-May), (2) summer (June–August), (3) autumn (September–November), and winter (December– February). The locations of the three sites are depicted in Fig. 1.

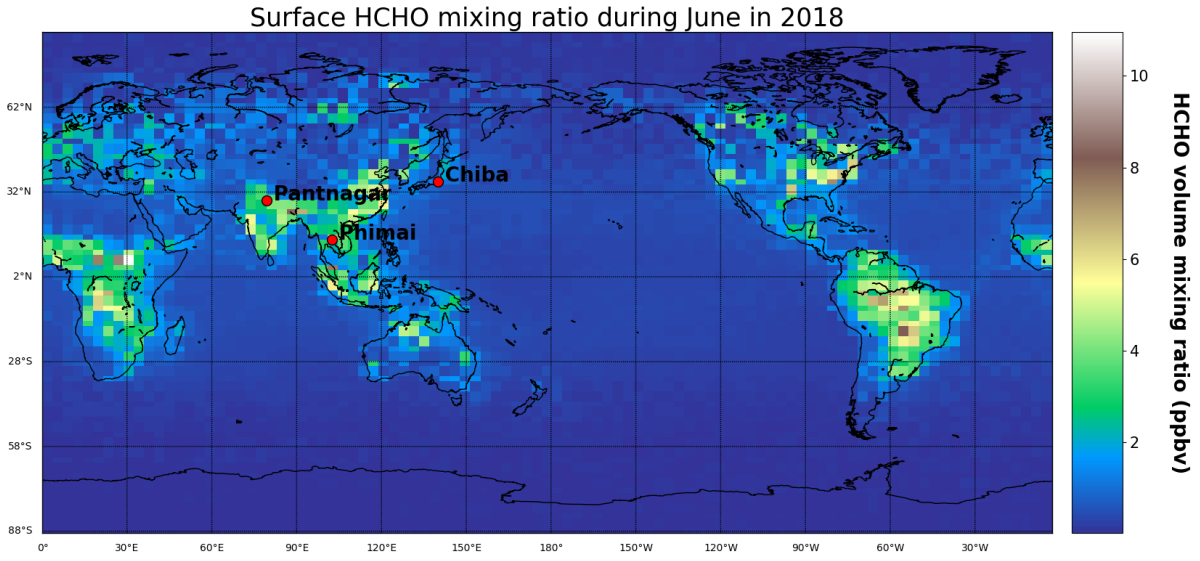

Figure 1: Surface HCHO mixing ratio during June 2018, simulated using the CHASER model. The red points represent locations of the observation sites, which are part of the A-SKY network.

2.2 MAX-DOAS retrieval

The MAX-DOAS systems used for continuous observations at the three sites participated in the Cabauw Intercomparison Campaign of Nitrogen Dioxide measuring Instruments (CINDI) (Roscoe et al., 2010) and CINDI-2 (Kreher et al., 2020) campaigns. The instrumentation setup is described by Irie et al. (2008, 2011, 2015). The indoor part of the MAX-DOAS systems consists of an ultraviolet-visible (UV-VIS) spectrometer (Maya2000Pro; Ocean Optics Inc.) embedded in a temperature-controlled box. The outdoor unit consists of a single telescope and a 45° inclined movable mirror on a rotary actuator, used to perform reference and off-axis measurements. The high-resolution spectra from 310–515 nm is recorded at six elevation angles (ELs) of 2°, 3°, 4°, 6°, 8°, and 70° at the Chiba and Phimai sites. At the Pantnagar site, measurements are conducted at ELs of 3°, 4°, 5°, 6°, 8°, and 70°. The sequences of the ELs at all the sites were repeated every 15 min. The reference spectra are recorded at EL of 70° instead of 90° to avoid saturation of intensity. Because all the ELs were considered in the box air mass factor (A_{box}) calculation to retrieve the vertical profile, the choice of reference EL (70˚ or 90˚) is not an important issue for this study. The off-axis ELs are limited to < 10° to reduce the systematic error in the in-oxygen collision complex (O_4) fitting results (Irie et al., 2015), thereby maintaining high sensitivity in the lowest layer of the retrieved aerosol and trace gas profiles. Daily wavelength calibration using the high-resolution solar spectrum from Kurucz et al. (1984) is performed to account for the spectrometer's long-term degradation. The spectral resolution (full width half maximum: FWHM) is about 0.4 nm at 357 and 476 nm. The concentrations and profiles of aerosol and trace gases are retrieved using the Japanese vertical profile retrieval algorithm (JM2 ver. 2) (Irie et al., 2011, 2015). The algorithm works in three steps: (1) DOAS fittings, (2) profile/column retrieval of aerosol, and (3) profile/column retrieval of trace gases. Irie et al. (2008a, 2008b, 2011, 2015) described the retrieval procedures, and the error estimates. Herein we provide a short overview.

First, the differential slant column density (ΔSCD) of trace gases is retrieved using the DOAS technique (Platt 1994), which uses the nonlinear least-squares spectral fitting method, according to the following equation :

$$lnI(\lambda) = ln(I_o(\lambda) - c(\lambda)) - \sum_{i}^{n} \sigma_i(\lambda)\Delta SCD_i - p(\lambda) \quad (1)$$

Therein, $I_o(\lambda)$ represents the reference spectrum measured at time *t*. $I_o(\lambda)$ is derived by interpolating two reference spectra (i.e., EL=70°) within 15 min before and after the complete sequential scan of the off-axis ELs at time *t*. ΔSCD represents the difference between the slant column density along the off-axis and reference spectrum. Second- and third-order polynomials are fitted to account, respectively, the wavelength-dependent offset $c(\lambda)$ and the effect of molecular and particle scattering $p(\lambda)$. In addition, $c(\lambda)$ accounts for the influence of stray light. The HCHO ΔSCD and NO_2 ΔSCD are retrieved respectively, from the fitting windows of 340–370 and 460–490 nm. Significant O_4 absorptions in the 338–370 and 460–490 nm fitting windows are used to retrieve the O_4 ΔSCDs. The absorption cross-section data sources and the fitted absorbers in the HCHO and NO_2 fitting windows are given in Table 1. Figure 2 presents an example of the fitting results. O_4 fittings in both retrieval windows are shown in Fig S1 (supplementary information).

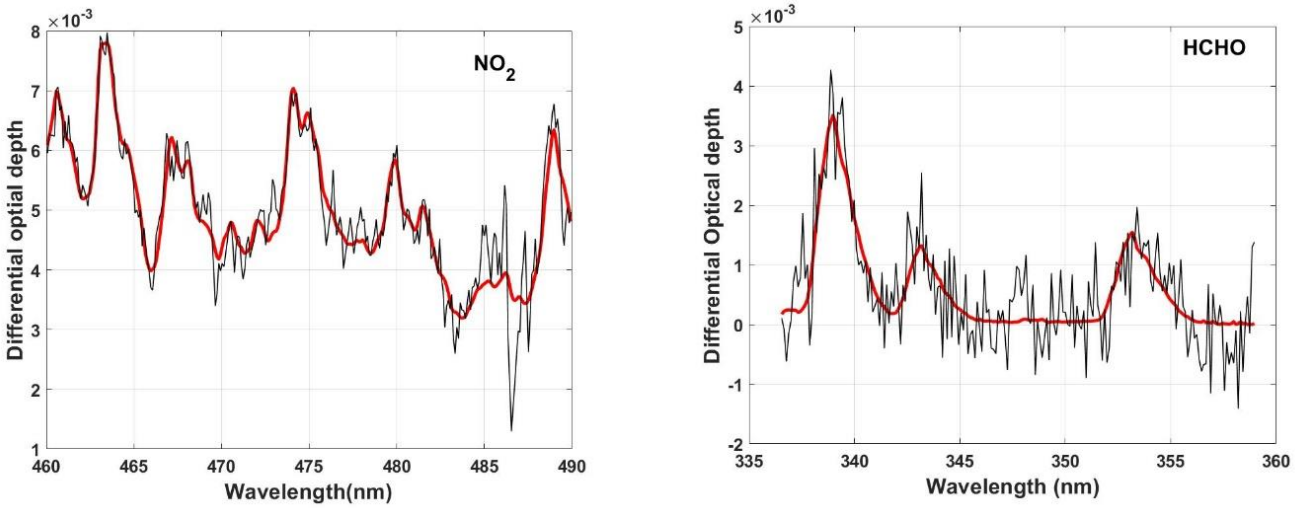

Figure 2: Examples of spectral fitting of NO_2 and HCHO, where red and black lines respectively show the scaled cross-section and the summation of scaled cross-sections and fitting residuals, respectively. The example shows the measurements on 10 April 2017, in Phimai at 10:00 LT at an EL of 2°.

In the second step, the aerosol optical depth (AOD) τ and the vertical profiles of the aerosol extinction coefficient (AEC) k are retrieved using the approach developed by Irie et al, (2008a) which is based on the optimal estimation method (Rogers, 2000). In this approach, the measurement vector y (representing the quantities to be fitted) and state vector (representing the retrieved quantities) is defined as

$$y = (O_4\Delta SCD(\Omega_1) \dots \dots \dots \Delta SCD(\Omega_n))^T \quad (2) \text{ and}$$

$$x = (\tau F_1 F_2 F_3)^T \quad (3),$$

Table 1. Cross-section data references and absorbers fitted in the HCHO and NO_2 windows

Cross-section	Absorbers fitted	Data Source
O_3		Bougmil et al. (2003), 223K
NO_2	O_3, NO_2, H_2O, O_4, Ring	Vandaele et al. (1996), 295K
BrO		Fleischmann et al. (2004), 223K
Ring		Chance and Spurr (1997)
H_2O		Vandaele et al. (2005), 280K
O_4		Hermans et al. (2003), 296K
HCHO	O_3, NO_2, HCHO, BrO, O_4, Ring	Meller and Moortgart (2000), 293k

where n stands for the number of measurements within one complete scan of an EL sequence. Also, Ω denotes the viewing geometry and includes three components: solar zenith angle (SZA), EL, and relative azimuth angle (RAA). The F values determine the profile shape, with values between 0 and 1. The partial AOD for 0–1, 1–2, 2–3, and above 3 km layers were defined respectively as AOD $\cdot F_1$, AOD $\cdot(1-F_1)\,F_2$, and AOD $\cdot\,(1-F_1)\,(1-F_2)\,F_3$, and AOD $\cdot(1-F_1)\,(1-F_2)\,(1-F_3)$. The AEC profile from 3 to 100 km is derived

assuming a fixed value at 100 km and exponential AEC profile shape with a scaling height of ~1.6 km. The k value at 100 km was estimated from Stratospheric Aerosol and Gas Experiment III (SAGE III) aerosol data (λ=448 and 521 nm) taken at altitudes of 15–40 km. The non-substantial influence of such assumptions on the retrievals in the lower troposphere has been demonstrated in sensitivity studies reported by Irie et al (2012). Similarly, the AEC profiles at 2–3, 1–2, and 0–1 km were derived. Such parameterization provides the advantage that the AEC profile can be retrieved using only the apriori knowledge of the *F* values (profile shape) and little or no information related to the absolute AEC values in the troposphere. Irie et al. (2008a) demonstrated that the relative variability of the profile shape, in terms of 1-km averages, is smaller than that of the absolute AEC values. AEC profile shapes corresponding to different *F* values is shown in Fig.S2 (supplementary information). However, the vertical resolution and the measurement sensitivity cannot be derived directly with such a parameterization (Irie et al., 2008a; 2009). The retrievals and simulations conducted by other groups for similar geometries (i.e., Frieß et al., 2006) are used to overcome such limitations. The apriori values used for this study were similar to those reported by Irie et al. (2011): AOD = 0.21 ± 3.0, F_1 = 0.60 ± 0.05, F_2 = 0.80 ± 0.03, and F_3 = 0.80 ± 0.03.

Then, a lookup table (LUT) of the box air mass factor (A_{box}) vertical profile at 357 and 476 nm is constructed using the radiative transfer model JACOSPAR (Irie et al., 2015), which is based on the Monte Carlo Atmospheric Radiative Transfer Simulator (MCARaTS) (Iwabuchi, 2006). The values of the single-scattering albedo (s), asymmetry parameter (g), and surface albedo were, respectively, 0.95, 0.65 (under the Henyey-Greenstein approximation), and 0.10. The U.S. standard atmosphere temperature and pressure profiles were used for radiative transfer calculations. Uncertainty of less than 8% related to the usage of fixed values of s, g, and a were estimated from sensitivity studies (i.e., Irie et al 2012). Results obtained from JACOSPAR are validated in the study reported by Wagner et al. (2007). The optimal aerosol load and the A_{box} profiles are derived using the A_{box} LUT and the O_4 ΔSCD at all ELs.

In the third step, the A_{box} profiles, HCHO and NO_2 ΔSCDs, and the nonlinear iterative inversion method are used to retrieve the HCHO and NO_2 vertical column densities (VCDs) and profiles. Here the NO_2 retrieval is explained.

For trace gas retrieval, the measurement vector and state vector are defined as

$$y = (NO2\Delta SCD(\Omega_1) \dots \dots \dots NO2\Delta SCD(\Omega_n))^T \quad (4)$$ and

$$x = (VCDf_1f_2f_3)^T \quad (5)$$

VCD represents the vertical column density below 5 km. The *f* values are the profile shape factors. Above the 5 km layer, fixed profiles are assumed. Similarly, to aerosol retrieval, the partial VCD values for the 0–1, 1–2, 2–3, and 3–5 km is defined respectively as VCD ·f_1, VCD ·(1-f_1) f_2, VCD · (1-f_1) (1-f_2) f_3, and VCD ·(1-f_1) (1-f_2) (1-f_3). Finally, the volume mixing ratio (VMR) is calculated using the partial VCD, and U.S. standard atmosphere temperature and pressure data scaled to the respective surface measurements.

The calculated vertical profile is converted to NO_2 ΔSCDs using the A_{box} LUT constructed for aerosol retrieval. However, the trace gas wavelengths differed from the representative wavelengths of A_{box} LUT (357 and 476 nm). Therefore, the AOD at the trace gas wavelength is estimated, converting the retrieved AOD to the closer aerosol wavelength of 357 or 476 nm, assuming the Angstrom exponent value of 1.00. The choice of the Angstrom exponent value can induce uncertainty in the retrieved VCDs. However, such uncertainty was found to be non-significant compared to that of A_{box} profiles. Uncertainty in the A_{box} profiles are assumed to as high as 30 to 50%. Such values are derived empirically from comparison with sky radiometer and LIDAR observations (i.e., Irie et al., 2008b). Then, the A_{box} profiles from the LUT corresponding to the recalculated AOD values are selected. The dependence of the A_{box} profiles on the concentration profiles is expected to be low because both HCHO and NO_2 are optically thin absorbers (Wagner et al., 2007; Irie et al., 2011). For every 15 min (time necessary for one complete scan of ELs), 20% (the mean ratio of the retrieved VCD to maximum ΔSCD) of the maximum trace gas ΔSCDs is used as a priori information for the VCD retrievals. The a priori error is set to 100% of the maximum trace gas ΔSCD. Figure 3 presents the mean averaging kernel (AK) of the HCHO and NO_2 retrievals during the dry season at Phimai. The area (Rodgers, 2000) provides an estimate of the measurement contribution to the retrieval. The total area is the sum of all the elements in the AK and weighted by the a priori error (Irie et al. 2008a). The areas for VCD and *f1* of NO_2 retrieval are 1 and 0.6, respectively. The *f2* and *f3* values are much smaller. Consequently, at first, the a priori profiles were scaled, and later *f* values determined

the profile shape. The VCD area is close to unity, and therefore, the retrieved VCD is independent of the a priori values. Irie et al (2008) conducted sensitivity studies of choice of the *f* values and reported negligible effect on the retrievals.

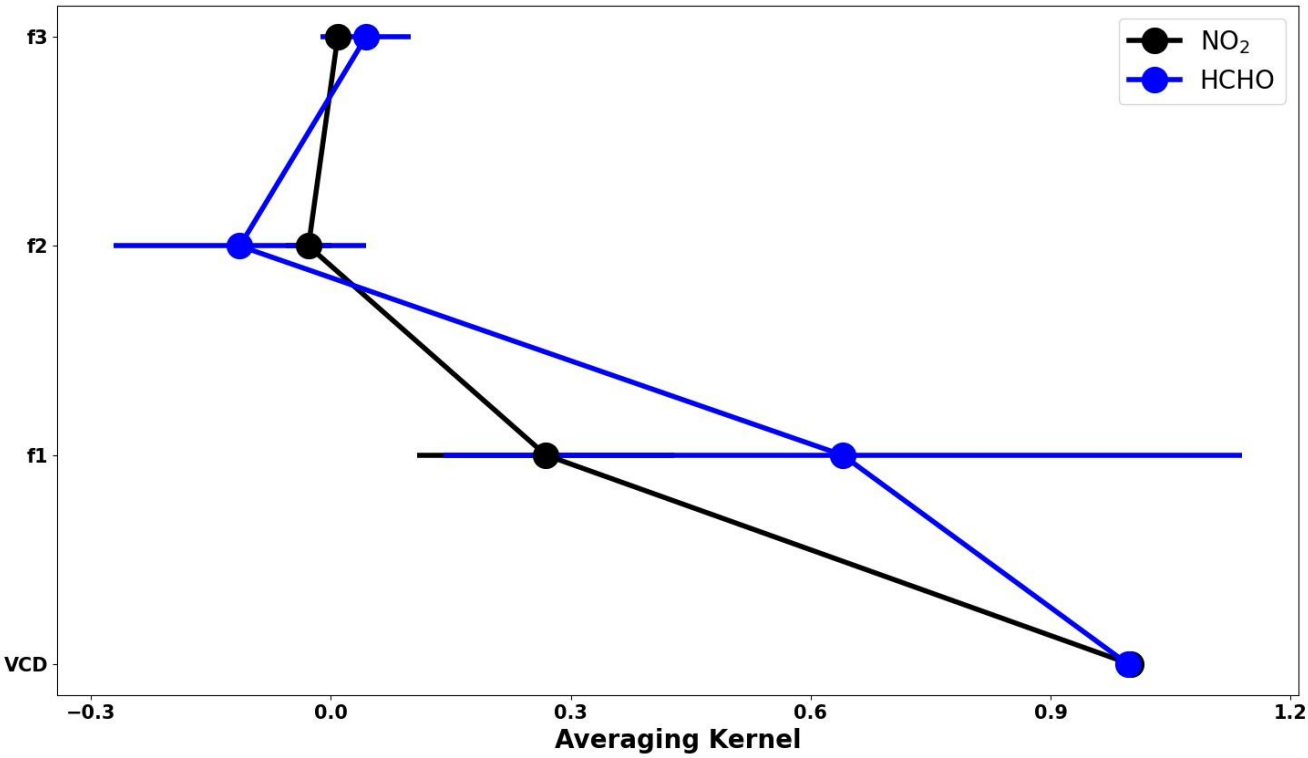

Figure 3: Mean averaging kernel of the NO_2 and HCHO retrievals from observations at Phimai during 2017

The total error of the retrieval consists of random and systematic errors. The measurement error covariance matrix constructed from the residuals of the respective trace gas ΔSCDs is used to estimate the random error. The systematic error is calculated while assuming uncertainties as high as 30 and 50% in the retrieved AOD (or the corresponding A_{box} values). Table 2 shows the total estimated error. Aside from the random and systematic error, more sources of error might exist. For instance, the bias in the ELs can induce uncertainties in the retrieved products. However, Hoque et al. (2018) demonstrated that such biases had a non-significant effect on the final retrieved products, mostly less than 5%.

The cloud screening procedure is similar to that described by Irie et al. (2011) and by Hoque et al. (2018a, 2018b). During the retrieval steps, retrieved AOD values greater than 3 are excluded, because optically thick clouds are primarily responsible for such large optical depth. Filtering based on the residuals of O_4 and the trace gas ΔSCDs is also used to screen clouds. The screening criteria are: respective residuals of O_4, HCHO, and NO_2 ΔSCDs < 10%, < 50%, and <20%, and the degrees of freedom of retrievals greater than 1.02. The threshold values were determined statistically corresponding to the mode plus one sigma (1σ) in the logarithmic histogram of relative residuals.

Table 2. Estimated Errors (%) for the NO_2 and HCHO concentration in 0-1 km layer, retrieved using the JM2 algorithm

Retrieved Product	Random error	Systematic error	Error related to instrumentation	Total error
NO_2	10	12	5	16
HCHO	16	25	5	30

2.3 CHASER simulations

CHASER 4.0 (Version 4) (Sudo et al., 2002; Sudo and Akimoto, 2007; Sekiya and Sudo, 2014), coupled online with the MIROC-AGCM atmospheric general circulation model (AGCM) (K-1 model developers, 2004) and the SPRINTARS aerosol transport model (Takemura et al., 2005, 2009), is a global chemistry transport model used to study the atmospheric environment and radiative forcing. In addition, several updates, including the introduction of aerosol species (sulfate, nitrate, etc.) and related chemistry, radiation, and cloud processes, have been implemented in the latest version of CHASER.

CHASER can calculate the concentrations of 92 species through 263 chemical reactions (gaseous, aqueous, and heterogeneous chemical reactions) considering the chemical cycle of O_3–HO_x – NO_x –CH_4– CO along with oxidation of non-methane volatile organic compounds (NMVOCs)(Miyazaki et al., 2017). The chemical mechanism is largely based on the master chemical mechanism (MCM,

http://mcm.york.ac.uk)(Jenkin et al., 2015). CHASER simulates the stratospheric O_3 chemistry considering the Chapman mechanisms, catalytic reactions related to halogen oxides (HO_x, NO_x, ClO_x, and BrO_x), and polar stratospheric clouds (PSCs). Resistance-based parameterization (Wesely, 1989), cumulus convection, and large-scale condensation parameterizations are used to calculate dry and wet depositions. The piecewise parabolic method (Colella and Woodward, 1984)

Table 3: Settings of the CHASER simulations used in this study

Simulation	**Anthropogenic emissions**	**Pyrogenic emissions**	**Biogenic emissions**	**Soil NO_x emission**	**Other physical and chemical processes**
Standard	ON	ON	ON	ON	ON
L1_HCHO	ON	Pyrogenic VOCs switched	ON	ON	ON
L1_opt	ON	OFF	Reduced by 50%	ON	ON
L1_NO_2	ON	ON	ON	OFF	ON
L2	Anthropogenic VOC emissions switched OFF	ON	ON	ON	ON

and the flux-form semi-Lagrangian schemes (Lin and Rood, 1996) calculate advective tracer transport. CHASER simulates tracer transport on a sub-grid scale in the framework of the prognostic Arakawa–Schubert cumulus convection scheme (Emori et al., 2001) and the vertical diffusion scheme (Mellor and Yamada, 1974). In this study, CHASER simulations were conducted at a horizontal resolution of 2.8° × 2.8°, with 36 vertical layers from the surface to ~50 km altitude and a typical time step of 20 min. The meteorological fields simulated by MIROC-AGCM were nudged toward the six-hourly NCEP FNL reanalysis data at every model time step.

The anthropogenic, biomass burning, lightning, and soil emissions of NO_x were incorporated into CHASER simulations. Anthropogenic emissions were based on HTAP_v2.2 for 2008. Biomass burning and soil emissions from the ECMWF/MAC (Global Fire Assimilation System (GFAS)) reanalysis were used. The biogenic emissions for VOCs are based on the process-based biogeochemical model the Vegetation Integrative SImulator for Trace gases (VISIT) (Ito and Inatomi, 2012) simulations. The NO_x production from lightning is calculated based on the parameterization of Price and Rind (1992) linked to the convection scheme of the AGCM (Sudo et al., 2002). Isoprene, terpene, acetone, and ONMV emissions estimates in the VISIT inventory during July were 2.14×10^{-11}, 4.43×10^{-12}, 1.60×10^{-12}, and 9.93×10^{-13} $kgCm^{-2}s^{-1}$. Global NO_x emissions of 43.80 $TgNyr^{-1}$ are used in the simulations, considering industries (23.10 $TgNyr^{-1}$), biomass burning (9.65 $TgNyr^{-1}$), soil (5.50 $TgNyr^{-1}$), lightning (5 $TgNyr^{-1}$), and aircrafts (0.55 $TgNyr^{-1}$) as significant sources. Global isoprene emissions from vegetation were set to 400 $TgCyr^{-1}$.

NO_x emissions in India were estimated as 14 Tg/yr in 2016, almost two-fold increase since 2005 (~8 Tg/yr), with the energy and transportation sector being the largest contributor (Sadavarte et al 2014). Indian anthropogenic non-methane VOCs (NMVOCs) emissions in 2010 were estimated ~ 10 Tg/yr , with respective contributions of 60, 16, and 12% from residential, solvents, and the transport sector(Sharma et al 2015). In Japan, vehicular exhausts (14 - 25%), gasoline vapor (9 - 16%), liquefied natural gas (7 - 10%), and liquefied petroleum gas (49 - 71%) contribute to the total VOC concentrations (Morino

et al., 2011), with annual NMVOC emission of ~2 Tg (Kannari et al., 2007). Annual NO_x emissions in Japan and Thailand in 2000 was estimated as ~2000 and 591 kt/yr, with the largest contribution from transport-oil use, followed by the energy and industrial sector (Ohara et al., 2007). Annual anthropogenic VOC emissions in Thailand are approximately 0.9 Tg, with 43, 38, and 20% contributed, respectively, from industrial, residential and transportation sectors (Woo et al; 2020).

Multiple CHASER simulations with different settings used for sensitivity studies are presented in Table 3.

2.4 Satellite observations

Tropospheric NO_2 and HCHO retrievals from the Ozone monitoring Instrument (OMI) were also used to evaluate the model simulations. The ultra-violet nadir-viewing spectrometer OMI, on board the Aura satellite measures backscattering solar radiation covering the spectral range of 270 – 500 nm (Levelt et al., 2006). In an ascending sun-synchronous polar-orbit, OMI crosses the equator at 13:40 LT (local time (Zara et al., 2018). OMI measures at a spatial resolution of 13×24 km^2 and provides daily global coverage of various trace gases including NO_2 and HCHO. The NO_2 and HCHO datasets were obtained respectively from the TEMIS (www.temis.nl, last accessed on 2022/04/23) and aeronomie (https://h2co.aeronomie.be/, last accessed 2022/05/03) websites. For analysis, NO_2 tropospheric columns retrieved using the DOMINO version 2.0 (Boersma et al., 2011) algorithm were used for the analysis. Data meeting the following criteria were selected: cloud fraction < 0.5, SZA < 70˚, surface albedo < 0.3, quality flags =0, and cross-track quality flags= 0. For HCHO, we used the BIRA-IASB v14 (De Smedt et al 2015) retrieved products. The data filtering criteria was the following: cloud fraction < 0.4, SZA<70˚, AMF > 0.2, quality flag=0, and cross-track quality flag =0.

3 Results and discussion

3.1 Results from MAX-DOAS observations

3.1.1 HCHO seasonal variation

The monthly mean HCHO mixing ratios in the 0–1 and 0–2 km layers from January 2017 – December 2018 and the corresponding one sigma (1σ) standard deviations signifying the variation ranges for the three sites are presented in Fig. 4. The HCHO levels at the Phimai site show a consistent seasonal cycle, characterized by high VMRs during the dry season. Such enhancement is related to the influence of biomass burning during the dry season, which has been well documented in the work of Hoque et al. (2018). The HCHO mixing ratio at Phimai reach a peak in March or April, with a maximum of 4 – 6 ppbv. The variation in the peak concentration and timing depends mainly on the intensity of biomass burning activities. During the wet season, the HCHO concentrations are mostly within 2–3 ppbv, indicating a two-fold increase in HCHO abundances during the dry season. The daily mean HCHO amounts (0 –1 km) are 0.78 - 9.84 ppbv, representing seasonal modulation of 134%.

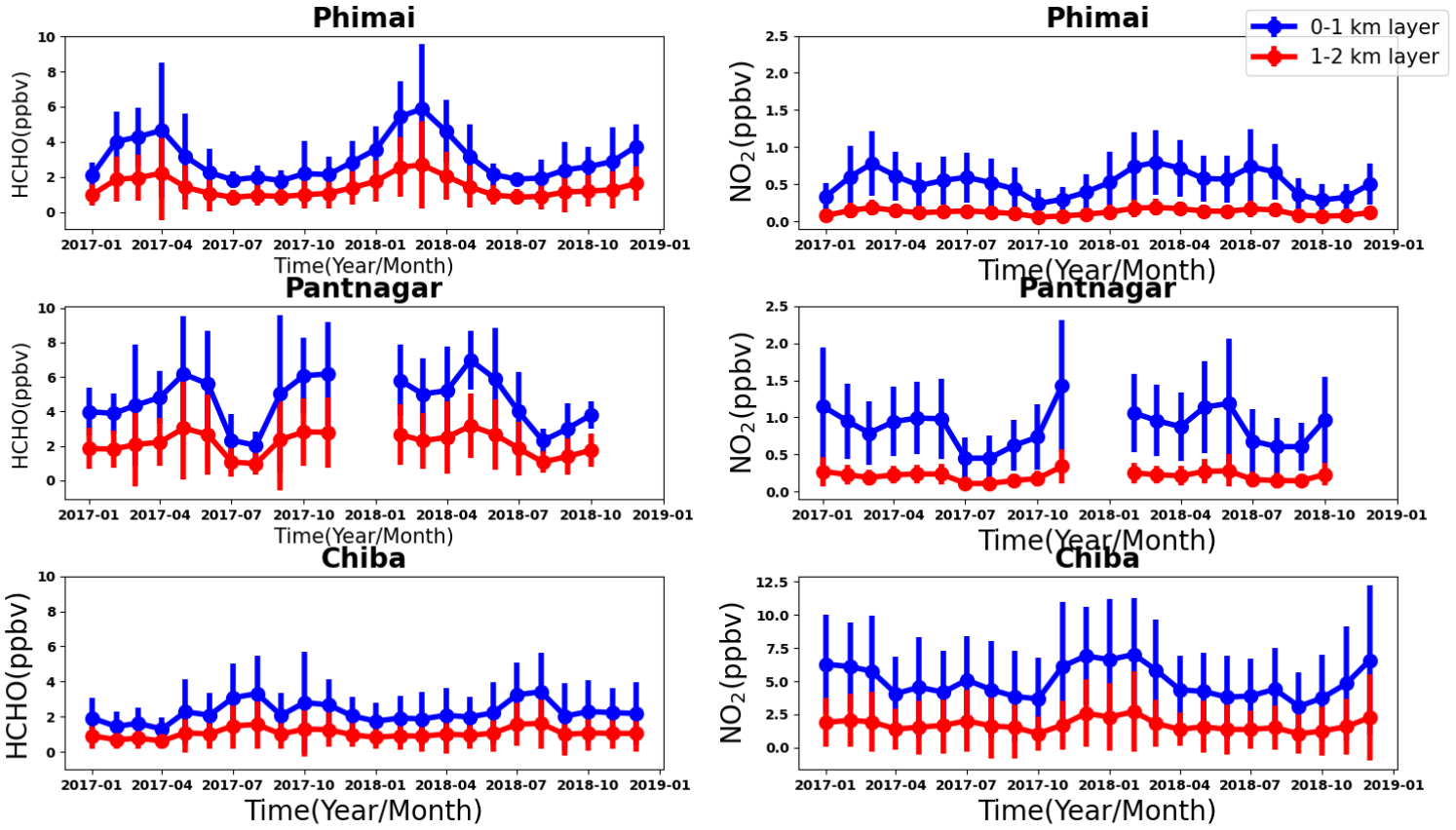

Figure 4: Seasonal variations in the HCHO (left panel) and NO_2 (right panel) mixing ratios in the 0 - 1 (blue) and 1 - 2 (red) km layers at Phimai, Pantnagar, and Chiba. The error bars represent the one sigma standard deviation of the mean values. The gaps in the plots for the Pantnagar site indicate the unavailability of observations during the investigated period.

Seasonal variation of HCHO in the 0–1 km layer at the Pantnagar site has been elucidated by Hoque et al. (2018b). Here, the results are replotted to verify the consistency of the seasonal variations. Observations made during autumn 2018 were not available because of problem with the spectrometer. Consistent seasonal variation of HCHO abundances is observed at the Pantnagar site, with enhanced concentrations during the spring. The Pantnagar site is affected by biomass burning during spring and autumn (Hoque et al., 2018b), explaining the high mixing ratios found during spring. In both years, the maximum HCHO mixing ratios are ~6 ppbv. The springtime peak occured in May. The HCHO concentrations during the monsoon are ~35% lower than in the spring, indicating a strong effect of the monsoon on the HCHO concentrations found for Pantnagar. The seasonal modulation of HCHO at Pantnagar estimated from the daily mean concentrations is 107%. The peak HCHO mixing ratio at Pantnagar is almost twice that of in Pune city (~ 3 ppbv) (Biswas and Mahajan, 2021), a site in the IGP region. The HCHO seasonality at the two sites are found to be dissimilar, because of differences in the VOC sources, however, lower mixing ratios during the monsoon is consistent. From another site in the IGP region (i.e., Mohali), Kumar et al., (2020) reported lowest HCHO VCDs during March 2014 and 2015, attributing them to lower biogenic and anthropogenic VOC emissions. At Pantnagar, the lowest HCHO mixing ratios are observed during the monsoon. The rainfall events in the IGP region shows strong annual variability (Fukushima et al. 2019). Discrepancies between the sites might be related to the rainfall pattern.

Under the influence of biomass burning, the maximum monthly HCHO mixing ratios at Phimai and Pantnagar are similar (~6 ppb). The maximum instantaneous HCHO VMR during biomass burning influence in Phimai and Pantnagar are, respectively, 26 and 30 ppbv. Zarzana et al. (2017) reported HCHO abundances of ~60 ppbv in fresh biomass plumes in the US. The lower values obtained from our

measurements might be attributable to (1) more aged plumes intercepted by the MAX-DOAS instruments and (2) differences in the types of biomass fuel used. Comparison to reports of literature indicates that the retrieval of HCHO under biomass burning is reasonable.

The summertime maximum and wintertime minimum characterize the seasonal variations of HCHO at the Chiba site, with a peak at ~3 ppbv. The HCHO concentrations are ~2 ppbv during other seasons, which are similar to the HCHO concentrations in Phimai during the wet season. The seasonal variation amplitudes of HCHO at Chiba is ~94%. For a site with similar seasonal variation (i.e., summertime maximum and wintertime minimum), Franco et al. (2015) reported HCHO seasonal modulation of 88%.

The HCHO VMRs in the 1–2 km layers at all three sites are lower, almost 50% the value of the concentrations in the 0–1 km layer. The HCHO seasonal variation amplitudes at Phimai, Pantnagar, and Chiba sites are, respectively, 131%, 102%, and 90% when calculated based on the HCHO concentration in the 1–2 km layers. The modulation was even lower when retrieved values for the 2–3 km layer is used.

3.1.2 NO_2 seasonal variation at the three sites

Figure 4 also shows the seasonal variation of NO_2 in the 0–1 and 1–2 km layers at the three sites. The error bars represent the 1σ standard deviation of the mean values. The NO_2 seasonal variations at Phimai and Pantnagar sites are similar to those of HCHO. Pronounced peaks attributable to biomass burning influence is observed during the dry season at Phimai (~0.8 ppbv) and during spring (1.2 ppbv), and post-monsoon (1.4 ppbv) at Pantnagar. The lowest NO_2 mixing ratios at Phimai and Pantnagar are, respectively, ~0.2 and 0.5 ppbv. The NO_2 VMRs at Chiba is higher (~7 ppbv) during winter. The longer lifetime of NO_x and lower NO/NO_2 ratio because of lower photochemical activity in winter lead to high NO_2 mixing ratios at Chiba (Irie et al., 2021).

At Phimai, the NO_2 mixing ratios in both seasons are similar. However, when Hoque et al. (2018a) reported the seasonal variations in NO_2 at Phimai during 2015 – 2018, the dry season mixing ratios were higher. Table 4 shows the number of fire events during the dry seasons during 2015 - 2018. The fire data are extracted from the MODIS Active Fire Detections database (https://firms.modaps.eosdis.nasa.gov, last accessed on 2021/12/15). Data fulfilling the following criteria were chosen – (a) data points located within 100 km of the Phimai site, (b) confidence of the data greater than 70%, and (c) observations during the daytime. The lower fire counts during 2017 - 2018 compared to those of 2015 - 2016 period coincide

with the lower NO_2 levels in the former. Fire counts varied between 2017 and 2018 but did not affect the NO_2 levels. However, HCHO levels changed with the number of fire occurrences between 2015 – 2018 (i.e., Figure 4 and Hoque et al.,2018a).

At such low NO_2 levels at Phimai, soil NO_x emissions are likely to make a greater contribution to NO_2. Although NO_2 is not emitted directly from soils, biological processes emit NO, which is rapidly converted to NO_2 (Hall et al., 1996). In addition, many studies have established a relation between soil moisture and NO emissions (Carden et al., 1993; Zheng et al., 2000; Schindlbacher et al., 2004; Huber et al., 2020). The potential contribution of soil NO_x emissions, as inferred from CHASER simulations, is discussed in section 3.4.2.

Table 4: Number of fire events occurring during the dry season (January - April) at Phimai from 2015 - 2018. Selection criteria of the data are the following: (1) situated within 100 km of the site, (2) confidence level > 70%, and (c) daytime measurements.

Dry season years	Number of fire events
2015	84
2016	98
2017	62
2018	77

3.1.3.1 The HCHO to NO_2 ratio (R_{FN}):

The HCHO to NO_2 (R_{FN}) ratio is regarded as an indicator of high ozone O_3 sensitivity (Martin et al., 2004; Duncan et al., 2010). The O_3 production regime is characterized as VOC-limited for $R_{FN} < 1$ and NO_x-limited when $R_{FN} > 2$, and the values in the range 1-2 are said to be in the transition/ambiguous region (Duncan et al., 2010; Ryan et al., 2020). Subsequent to a report of Tonnesen and Dennis (2000), several studies used R_{FN} estimated from satellite and ground-based observations to infer O_3 sensitivity to NO_x and VOCs (Martian et al., 2004; Duncan et al., 2010; Jin and Holloway et al.,2015; Mahajan et al., 2015; Irie et al.,2021; etc.). However, the effectiveness of R_{FN} is still under discussion primarily based on two-points- (1) the range of the transition region to categorize the VOC and NO_x -limited region, and (2) the

altitude dependence of R_{FN} (Jin et al., 2017). Most of the studies described above used the transition range ($1 < R_{FN} < 2$) proposed by Duncan et al. (2010). Schroeder et al. (2017) reported that a common transition (i.e., $1 < R_{FN} < 2$) range might not be valid globally. Instead, it should be calculated based on the region. First, the results based on the standard transition range are discussed herein, and then its applicability to the study regions is assessed.

Figure 5 shows scatter plots of the daily mean NO_2 and HCHO concentrations in the 0 - 2 km layer at the three sites, color-coded with the respective O_3 concentrations (0-2 km). Retrieval of the JM2 O_3 product is explained by Irie et al. (2011). The O_3 concentrations for SZA < 50° are used to minimize stratospheric effects. The JM2 O_3 product showed good agreement with ozonesonde measurements (Irie et al., 2021). Most of the high O_3 occurrences fall in the $R_{FN} > 2$ region at Phimai and Pantnagar and in $R_{FN} < 1$ at Chiba. The common transition range classifies the O_3 production regime as NO_x-limited at Phimai and Pantnagar and VOC-limited at Chiba. At all sites, the R_{FN} values tend to be biased to a particular regime (i.e., NO_X - or VOC-limited), with only 4 and 2% of the ratios in the range 0 - 2, at Phimai and Pantnagar, respectively. This finding suggests that the transition occurs at a higher or lower ratio than the common definition. Recent report by Souri et al. (2020) found that the NO_2-HCHO relation plays an important role in determining the transition region and derived a formulation from accounting for the NO_2-HCHO chemical feedback in the ratios as

$$HCHO = m * (NO_2 - b) \quad (6)$$

where m and b respectively denote the slope and intercept. Equation (6) is based on observations, which means that the regionally adjusted fitting coefficients will reflect the local NO_2 - HCHO relation. Solving equation (6), the transition line estimated from the observations in the 0 - 2 km layer, is shown in Fig 5 (bottom panel). Rather than a range, the method calculates a single transition line, which corresponds to the NO_2 - HCHO feedback. The regions above and below the transition line are characterized, respectively as VOC- and NO_x -limited or other.

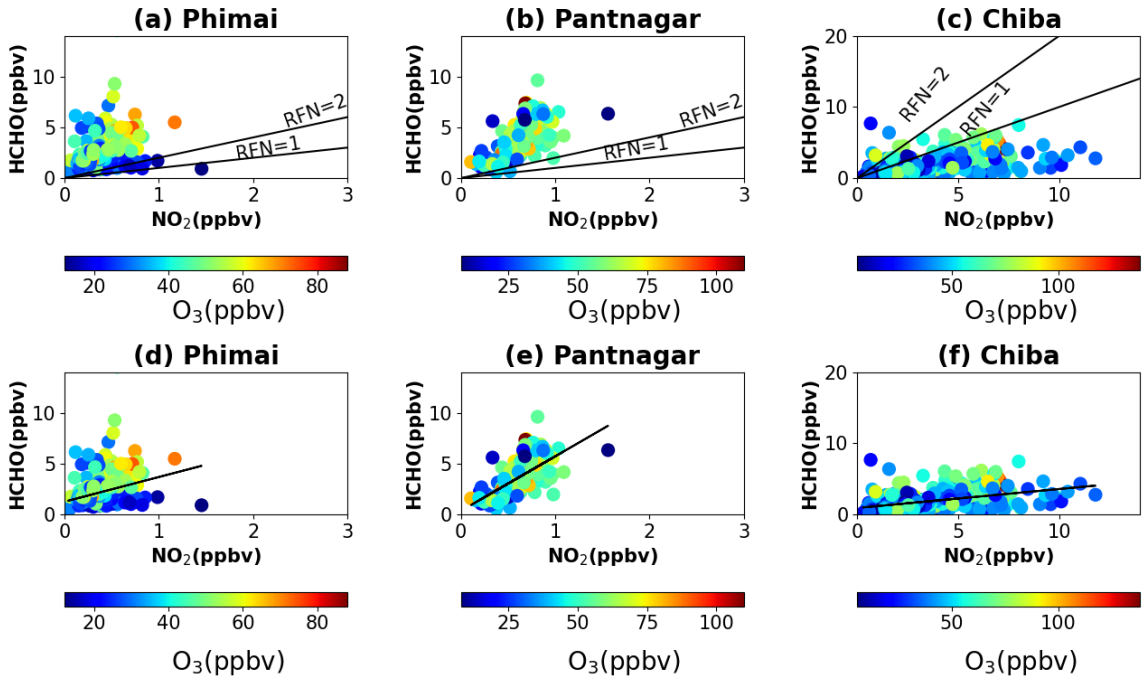

478

479 **Figure 5.** Scatter plots of HCHO and NO_2 concentrations in the 0-2 km layer at (a, d) Phimai, (b, e) Pantnagar, and
480 (c, f) Chiba, coloured with the O_3 concentrations in the 0-2 km layer at the respective sites. The solid lines in the
481 top panel represent R_{FN} = 2 and R_{FN} =1 benchmarks. The black lines in the bottom panel are calculated according
482 to equation (1).

483

484 The revised transition line at Phimai and Pantnagar is apparently more reasonable than the earlier method.
485 At Phimai, the transition line almost clearly distinguishes between the high and low O_3 occurrences. It is
486 perceptible that when the HCHO concentrations are higher than NO_2, the transition of the regimes is likely
487 to occur at higher R_{FN} values. The minimum and mean R_{FN} value along the transition line are 3.62 and
488 6.78, respectively. Because Phimai is a VOC-rich environment, the regime transition occurs at higher R_{FN}
489 values than by the conventional definition. This finding echoes the results reported by Schroder et al.
490 (2017) for a regionally variable transition region. The definition of R_{FN} <1 as a VOC -limited regime might
491 not be valid in this case. Considering the mean R_{FN} ratio along the transition line (i.e., 6.78), the VOC-

and NO_x -limited (and other) regimes are defined, respectively as R_{FN} <6.78 and R_{FN} >6.78. Based on this definition, around 34% (65%) of the ratios are higher (lower) than 6.78, classifying Phimai as a dominant VOC-limited region, which contradicts earlier results. Biomass burning affects Phimai during January - April and is a significant emission source in addition to biogenic emissions. Thus, high O_3 occurrences likely occur only 30% of the time during a year. Such events mostly lie above the transition line.

At Pantnagar, high O_3 occurrences lie below (42%) and above (57%) the transition line, indicating that O_3 production is sensitive to both HCHO and NO_2 which contradicts results reported by Biswas et al. (2019). Based on satellite and ground-based observations, the study estimated the R_{FN} values at a site in the IGP as > 4 and >2 respectively, and regarded the O_3 regime as NO_x-limited. Mahajan et al (2015) reported R_{FN} values of less than 1 over the IGP region signifying as a VOC-limited region. Pantnagar is a sub-urban site situated beside a busy road. Therefore, effects of anthropogenic emissions are expected year-round, especially with pyrogenic emissions during the spring and post-monsoon period. O_3 sensitivity to both NO_x and VOCs in the north-west IGP region has also been reported by Kumar and Sinha (2021). Therefore, the balance between the VOC and NO_x-limited region in the IGP is reasonable. The mean and minimum R_{FN} value along the transition line are, respectively, 5.59 and 6.09. The minimum value (i.e., 5.59) is higher than Phimai (3.26), suggesting higher VOC levels at Pantnagar, consistent with the observations.

At Chiba, 60% of the R_{FN} values lie below the transition line, suggesting a dominant VOC-limited region, which is consistent with the results reported by Irie et al. (2021). The minimum and the mean R_{FN} along the transition line are, respectively, 0.33 and 0.72. The transition occurs at a low R_{FN} value because of higher NO_2 levels. The fact that, 40% of the R_{FN} values are above the transition region suggests a moderate effect of HCHO on the O_3 sensitivity at Chiba.

Although the new classification results are apparently reasonable, they should be interpreted with care. Our current understanding of R_{FN} contradicts the classification of rural sites as VOC-limited. Despite the theoretical and observational evidence (i.e., Souri et al.,2020), the classification of regimes based on a single transition line is not yet well-established. Schroder et al. (2017) used regionally varying transition ranges. Moreover, (a) the number of observations and (b) the systematic and retrieval errors can affect the estimations and classifications. These findings are expected to contribute to the ongoing discussion

about the effectiveness of R_{FN}. However, the results support the idea of a regionally varying transition range.

3.1.3.2 R_{FN} profiles

Figure 6 shows the seasonal mean R_{FN} profiles at the three sites. Only the profiles during the high O_3 concentrations at the sites (i.e., March at Phimai, May at Pantnagar, and February at Chiba) are shown. The R_{FN} values are likely increase with height because of the lower vertical gradient of NO_2, than that of HCHO (Fig.4). It is particularly interesting that, the R_{FN} values are similar in the 1-2 km height under biomass burning conditions, suggesting a small variation in the HCHO loss rate in the particular layer. At both sites, the HCHO concentration at 1.5 km is about 3 ppbv. At Chiba, a considerable amount of NO_2 in the higher layers increases the ratio up to 2 km height. Beyond 2 km, the ratio variation at all sites is opposite that found for the surface. The gradient issue of R_{FN} has been discussed explicitly by Jin et al. (2017). They proposed a conversion factor to account for gradient differences in the surface and column-derived R_{FN} values, estimating the conversion factor from the model simulated surface and column abundances of NO_2 and HCHO. We adopt the method reported by Jin et al. (2017) for this study using the CHASER simulated NO_2 and HCHO concentrations and vertical columns.

First, CHASER simulated near-surface NO_2 and HCHO concentrations were converted to number density. The effective boundary layer height (E) (Halla et al., 2011; Jin et al., 2017) was estimated.

$$E_{NO_2} = \frac{NO_2\ total\ column}{NO_2\ near-surface\ number\ density} \quad (7)$$

$$E_{HCHO} = \frac{HCHO\ total\ column}{HCHO\ near-surface\ number\ density} \quad (8)$$

Therein, E_{NO_2} and E_{HCHO} respectively denote the effective boundary layer heights of NO_2 and HCHO. In the second step, the column to surface conversion factor (F) was calculated according to the following equation:

$$F = \frac{E_{HCHO}}{E_{NO_2}} \quad (9)$$

The seasonal variation of F for the three A-SKY sites and the associated 1σ standard deviation of the mean values are depicted in Fig. 7(c). The F values over East Asia reported by Jin et al. (2017) were ~2, without marked seasonal variation. CHASER estimated F values over Chiba range between 1–2.5, which is apparently reasonable, when compared with literature values. Values reported in literature for polluted regions (NO_2 > 2.5 molecules cm^{-2}) considered simulation data for 1–2 PM, but the estimates for this study used daytime (07:00 – 18:00) simulations.

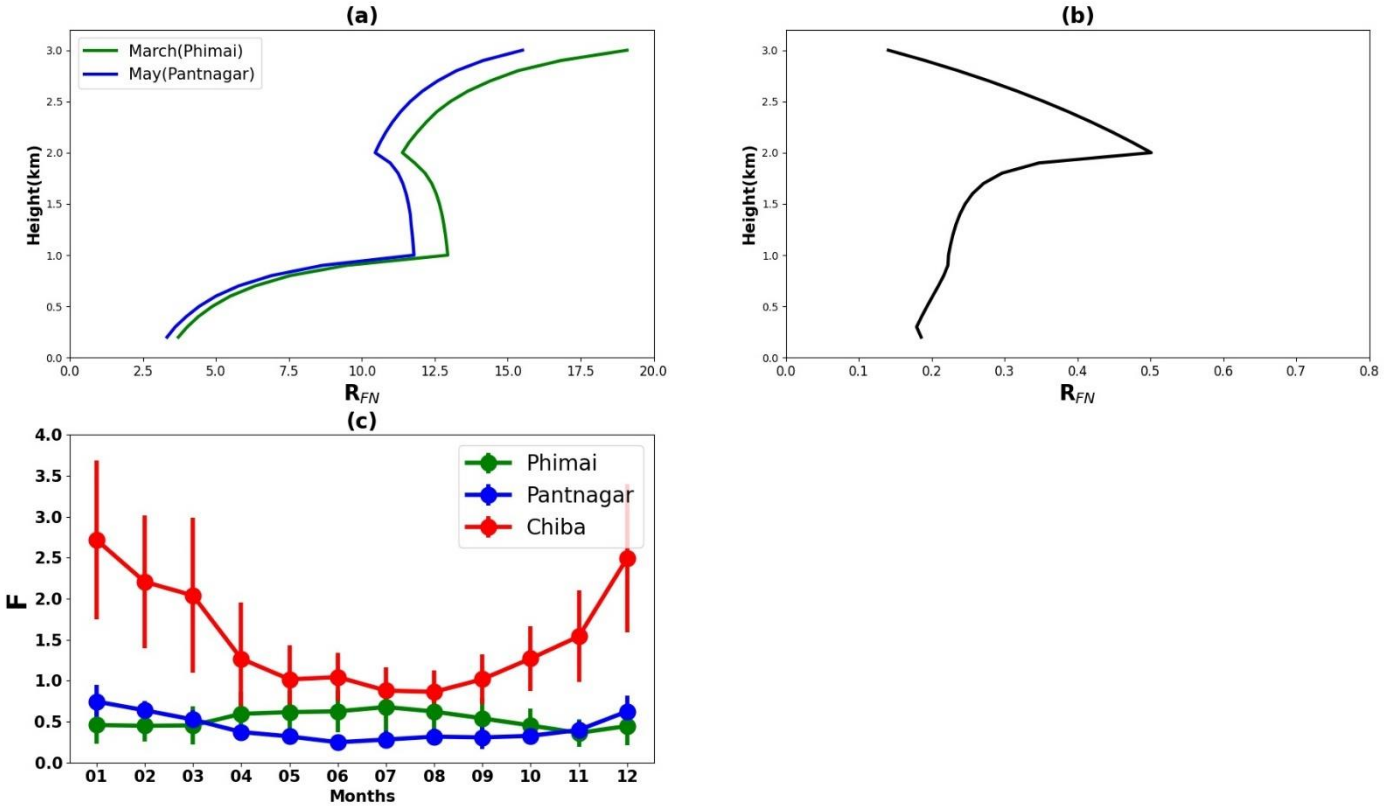

Figure 6: Seasonal mean R_{FN} profiles during (a) March and May at Phimai and Pantnagar, respectively, and (b) February at Chiba. (c) Seasonal variations in the column to surface conversion factor (F) for the Phimai, Pantnagar, and Chiba sites, estimated from the CHASER simulated HCHO and NO_2 surface concentrations and VCD. The simulated data from 07:00 – 18:00 in 2017 were used to estimate the F values. The error bars represent the one sigma standard deviation of the mean values.

The F values for Pantnagar are mostly less than 1, with no distinctive seasonal variation. Mahajan et al. (2015) reported OMI-derived R_{FN} values < 1 over the IGP region. When this estimated conversion factor is used with the values reported by Mahajan et al. (2015), the discrepancy in the satellite and ground-based observation derived R_{FN} values in the IGP region are reduced indicating that the estimated F values for the Pantnagar site can be representative for the IGP region. The F values at the Phimai site range were 0.5–1. Our estimated F values for the Phimai and Pantnagar sites are useful as representative values for these respective regions, which can be improved further based on the results.

3.2 Global Evaluation of the CHASER model

This section describes the evaluation of CHASER NO_2 and HCHO columns for 2017 against OMI observations. The OMI AKs were applied to the CHASER outputs to account for the altitude-dependence of the retrievals. First, 2-houly simulated profiles (NO_2 and HCHO) were sampled closest to the observation time. Secondly, AKs were applied to the sampled profiles and the mean profile was calculated. Thirdly, both the simulations and observations were averaged on a 2.8˚ bin grid. The month of July and December were discarded from the NO_2 comparison, because few observations (only five days) were available after filtering.

3.2.1 Comparison between CHASER and OMI NO_2

Figure 7 compares the simulated and observed annual mean tropospheric NO_2 columns. The statistics for the comparison are given in Table 5. The model captured the global spatial variation well with a spatial correlation (r) of 0.70. The mean bias error (MBE) and the root mean square error (RMSE) are respectively, 3×10^{14} and 5.4×10^{14} molecules cm^{-2}. On a global scale, CHASER estimations are negatively biased by 38% compared to OMI. Actually, studies evaluating global NO_2 simulations with satellite observations have reported similar negative biases (Miyazaki et al., 2012, Sekiya et al., 2018). The spatial representativeness between the model and observation is one potential reasons for such negative biases. However, CHASER simulations at 1.1˚ improved the MBE and RMSE by 5 and 15%, respectively, compared to simulations at 2.8˚ (Sekiya et al. 2018). Moreover, Sekiya et al (2018) used NO_2 simulations with an updated inventory and compared the results with OMI observations from 2014. Although they reported a better global spatial correlation ($r > 0.90$), the MBE (2.5×10^{14} molecules cm^{-2})

and RMSE (4.4×10^{14} molecules cm^{-2}) values at 2.8˚ resolution are comparable to those obtained from this study.

OMI retrievals show the highest NO_2 columns over eastern China (E-China) and Western Europe. Annual mean NO_2 columns over the remainder of the land areas are between 7×10^{14} and 4×10^{15} molecules cm^{-2}. Over the land areas the differences between the datasets are mostly between -2×10^{15} and 5×10^{14} molecules cm^{-2}. Although CHASER also underestimates NO_2 columns over the ocean, although the differences are lower than that of over lands. CHASER estimates are higher by $\sim5\times10^{14}$ molecules cm^{-2} than OMI over Japan. Since 2012, the NO_2 columns have shown a declining trend over Japan, mainly because of emission controls in China (Irie et al 2016). Probably because of simulations with an emission inventory earlier than 2012, the simulated values tend to be higher than observations.

Figure 8 compares the seasonal variations in the monthly mean NO_2 columns in some selected region. The error bars represent the 2-sigma standard deviation of the observed mean values. The numbers in each subplot signify the regional spatial correlation between the datasets. Over eastern China (E-China), CHASER values are negatively biased by 24%; the *r*-value is 0.68. The model captured the seasonality well within variation range of the observations. Over E- and W-USA (eastern and western USA), the respective *r*-values are 0.85 and 0.49 respectively. Simulated NO_2 columns are higher over E-USA than over W-USA, consistent with the observations. Although, in both regions model estimates are biased by ~23% in the lower side compared to OMI observations, the RMSE in E-USA are ~40% higher than in W-USA.

Over Europe, CHASER estimates are negatively biased by 54%, with an *r*-value and RMSE of 0.80 and 1.28×10^{15} molecules cm^{-2}, respectively. The observed NO_2 levels over Europe are almost twice those of the W-USA. The model was unable to capture the regional differences. Model underestimations in Europe can be attributed to the older anthropogenic emission inventory used for the study. In fact, using the HTAP 2010 inventory the MBE (-0.53 × 1015 molecules cm^{-2}) between OMI and CHASER NO_2 column

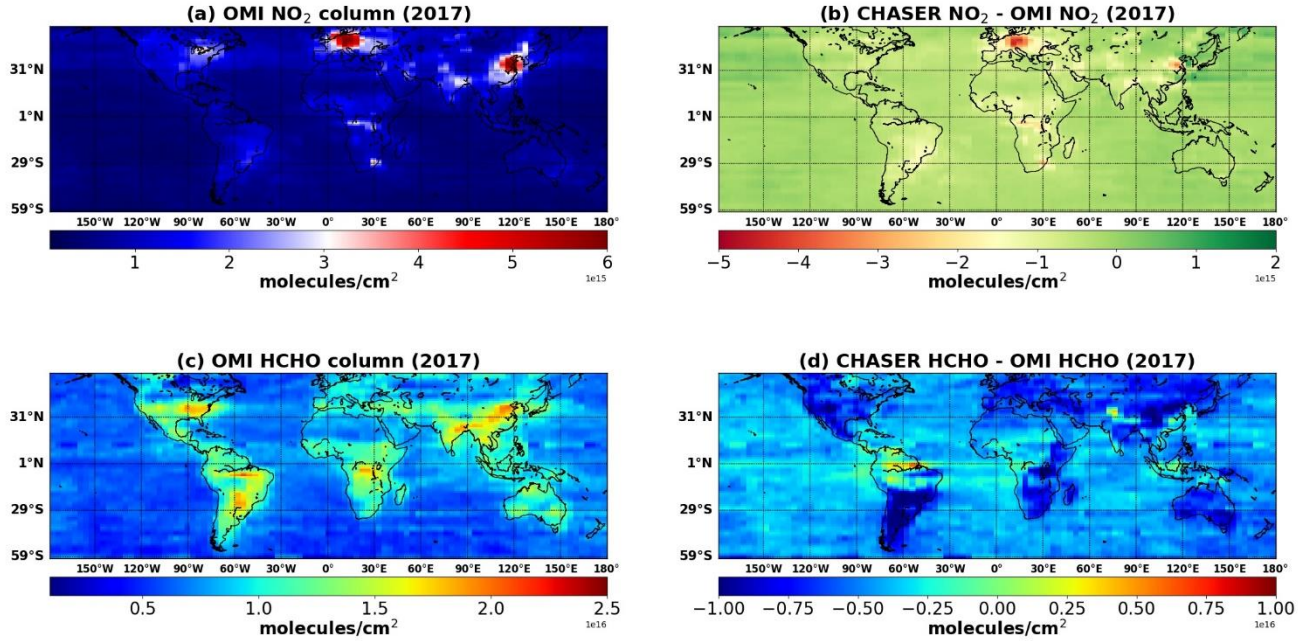

Figure 7: (first column) Annual mean tropospheric (a) NO_2 ($\times 10^{15}$ molecules cm^{-2}) and (c) HCHO ($\times 10^{16}$ molecules cm^{-2}) columns retrieved from OMI observations in 2017. Very limited NO_2 data in July and December met the filtering criterions, thus discarded from the calculation. (second column) The differences between the simulated and observed (c) NO_2 and (d) HCHO columns. All the datasets are mapped onto a 2.8˚ bin grid.

simulations at 2.8 over Europe (Sekiya et al. 2018), was ~ 50% lower than in the current study, although, their RMSE value is similar.

Over India, MBE and RMSE for the annual mean NO_2 column are -4.3×10^{14} and 4.4×10^{14} molecules cm^{-2}, respectively, and the *r*-value is moderate (0.65). Although CHASER estimates are negatively biased by

Table 5: Statistics of comparison of annual mean NO2 and HCHO columns between CHASER and OMI.MBE1 and MBE2 are the respective mean bias error. RMSE1 and RMSE2 are the respective root mean square errors. r1 and r2 signifies the respective spatial correlation coefficient. The units of MBE1 and RMSE1 are $\times 10^{15}$ molecules cm^{-2}. MBE2 and RMSE2 values are in the unit of $\times 10^{16}$ molecules cm^{-2}.

Region	r1 (CHASER vs OMI NO_2)	MBE1 (CHASER - OMI NO_2)	RMSE1 (CHASER – OMI NO_2)	r2 (CHASER vs OMI HCHO)	MBE2 (CHASER – OMI HCHO)	RMSE2 (CHASER – OMI HCHO)
Global	0.73	-0.30	0.54	0.74	- 0.45	0.49
E-China	0.68	-1.84	2.47	0.57	-0.63	0.64
E-USA	0.85	-0.62	0.63	0.91	-0.56	0.56
W-USA	0.49	-0.33	0.37	0.63	-0.71	0.71
Europe	0.80	-1.20	1.28	0.51	-0.67	0.68
India	0.65	-0.43	0.44	0.73	-0.56	0.57
N-Africa	0.58	-0.88	0.90	0.65	-0.29	0.32
S-Africa	0.80	-1.25	1.40	0.22	-0.66	0.70
S-America	0.87	-0.80	0.88	0.47	-0.31	0.40
SE Asia	0.57	-0.61	0.64	0.48	-0.41	0.44

32%, the values lie within the 2-sigma range of the observations. Sekiya et al. (2018) found no significant effect of higher model resolution on the MBE and RMSE in the Indian region.

Over N- and S-Africa (North and South Africa), the model values are biased low by more than 75% compared to the observations. Prominent biomass burning occurs in both regions, which explains the enhanced NO_2 levels in the OMI retrievals. High negative biases in the model values indicates that biomass burning NO_x emissions for the African regions are likely underestimated. Similarly, CHASER

underestimates NO_2 columns by 80% in South America, where pyrogenic emissions contributions are significant. CHASER estimates are lower than OMI in these regions, but model captured the spatial distribution well.

Over the SE-Asian (Southeast) region, OMI columns are enhanced during the dry season (i.e., January - April. Burning agricultural wastes is a common practice in many countries in Southeast Asia during the dry season, explaining the enhanced columns. The MBE (- 6 × 10^{14} molecules cm^{-2}) and RMSE (6.4 × 10^{14} molecules cm^{-2}) in the SE-Asia region are lower than the African regions (i.e., N-Africa, S-Africa, and S-America), where biomass burning is prominent.

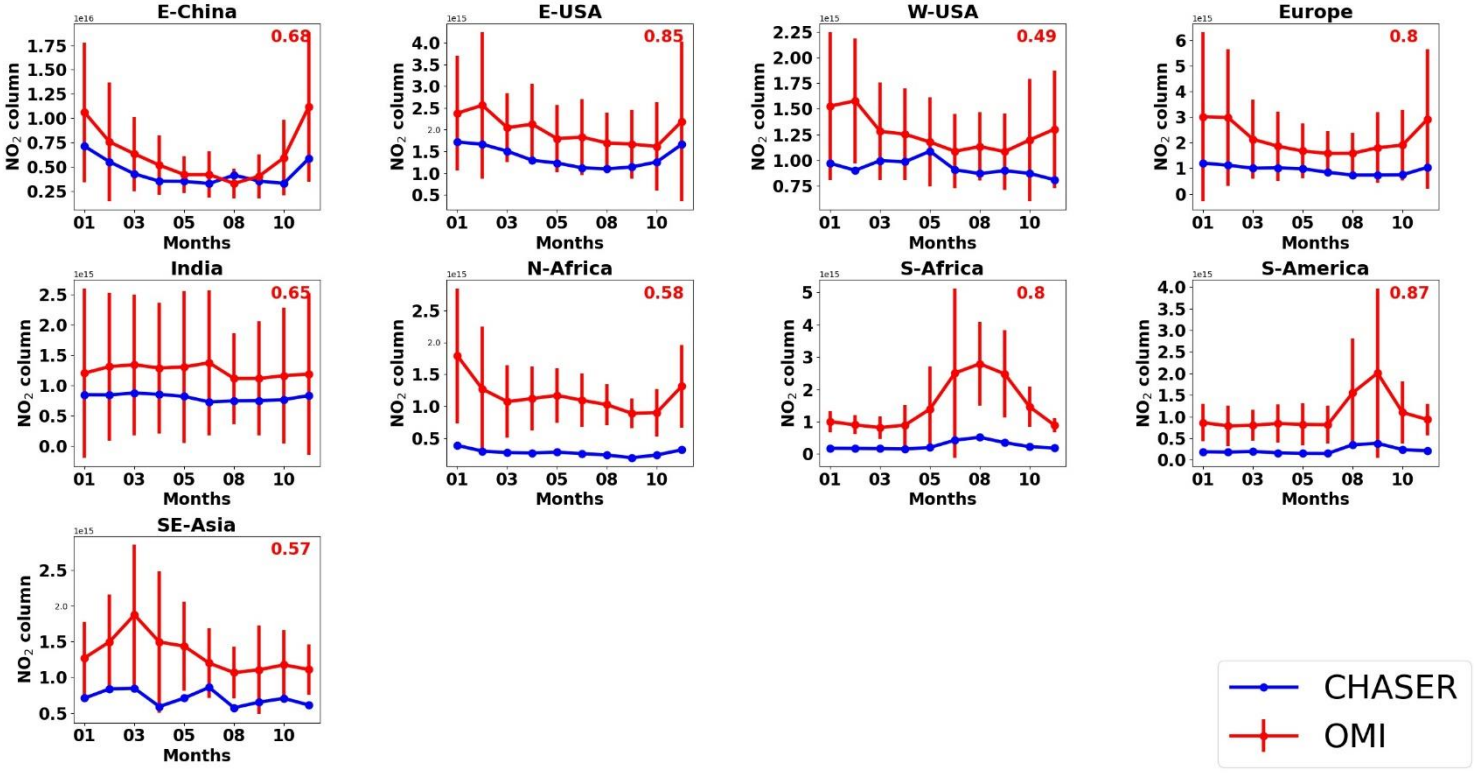

Figure 8: Seasonal variations in tropospheric NO_2 columns in E-China (110˚ -123˚ E, 30˚ – 40˚ N), E-USA (32˚ – 43˚ N, 71˚ – 95˚ W), W-USA(32˚ – 43˚ N, 100˚ – 125˚ W), Europe (35˚ – 60˚ N, 0˚ – 30˚ E), India (7.5˚ – 54˚ N, 68˚ – 97˚ E), N-Africa (5˚ – 15˚ N, 10˚ W – 30˚ E), S-Africa (5˚ -15˚ S, 10˚ -30˚ E), S-America (0˚ -20˚ S, 50˚ - 70˚ W), and SE-Asia (10˚ – 20˚ N, 9˚ – 145˚ E). CHASER simulations and OMI retrievals are plotted in blue and

red colors respectively. The error bars indicate the 2-sigma variation of the observed mean values. The number in the insets signifies the regional spatial correlation between CHASER and OMI NO_2 columns.

3.2.2 Comparison between CHASER and OMI HCHO

Figure 7 presents a comparison between the simulated and observed global annual mean HCHO columns. The statistics of the comparison are given in Table 5. CHASER is able to reproduce the observed global spatial variation well with r = 0.73. The global MBE and the RMSE are respectively, -4.5×10^{15} and 4.9×10^{15} molecules cm^{-2}. MBE and RMSE for monthly mean fields show no distinctive seasonal variation (Table S2). High HCHO columns are observed over China, Australia, Europe, India, Central Africa, South America, and the United States. The model mostly underestimated the HCHO abundances in the higher latitudes and Australia. Absolute differences between the model and observations in the higher latitudes vary between 5×10^{15} and 1×10^{16} molecules cm^{-2}. Figure 9 compares the seasonal variations in the monthly mean HCHO columns in some selected region. Therein error bars represent the 2-sigma standard deviation of the observed mean values. The numbers in the respective subplots signify the regional spatial correlation between the datasets.

Over E-China, CHASER HCHO estimates are negatively biased by 45% compared to OMI and the r-value is greater than 0.50. The model reproduced the observed HCHO seasonality well including enhanced peaks during the summer. The greatest differences between the datasets are observed during the winter. Over E-USA, the spatial correlation between the datasets is greater than 0.90. Also, the CHASER estimates are biased by 49% in the lower side. Simulations show that the peak in the HCHO abundances occurs in July, which is consistent with the observations. The observed and simulated magnitude of the seasonal modulation is 51 and 78%, respectively. The seasonality in the HCHO columns in E-China and E-USA signifies a strong contribution from biogenic emissions. In both regions, the observed peak HCHO column is ~ 1.75×10^{16} molecules cm^{-2}. The simulated peak HCHO values are also similar in both regions, despite the underestimation. Over W-USA and Europe, the negative biases in the simulation are greater than 60%. However, the simulated peaks during summer are consistent with the observations. The OMI retrievals show that the HCHO abundances in both regions are almost similar, which has been well captured by CHASER, although the magnitude is underestimated.

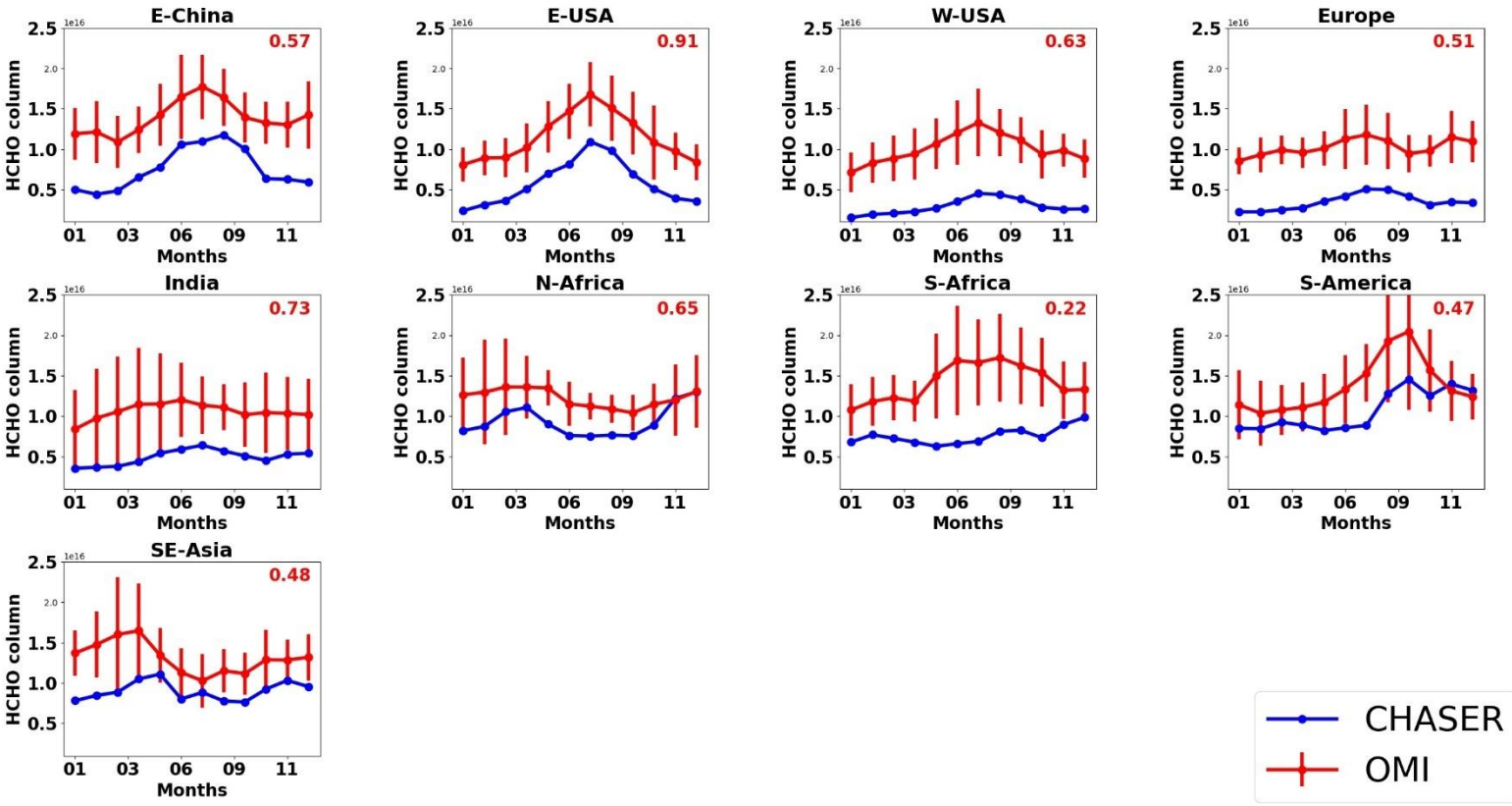

Figure 9: Seasonal variations in HCHO columns in E-China (110˚ -123˚ E, 30˚ – 40˚ N), E-USA (32˚ – 43˚ N, 71˚ – 95˚ W), W-USA(32˚ – 43˚ N, 100˚ – 125˚ W), Europe (35˚ – 60˚ N, 0˚ – 30˚ E), India (7.5˚ – 54˚ N, 68˚ – 97˚ E), N-Africa (5˚ – 15˚ N, 10˚ W – 30˚ E), S-Africa (5˚ -15˚ S, 10˚ -30˚ E), S-America (0˚ -20˚ S, 50˚ -70˚ W), and SE-Asia (10˚ – 20˚ N, 9˚ – 145˚ E). CHASER simulations and OMI retrievals are plotted in blue and red colors respectively. The error bars indicate the 2-sigma variation of the observed mean values. The number in the insets signifies the regional spatial correlation between CHASER and OMI HCHO columns.

Over India, the model estimates mostly lie outside of the observational variation ranges, although, CHASER captured the spatial distribution well (r = 0.73). Magnitudes of the seasonal variation in both OMI and CHASER are around 32%. Between the two African regions, CHASER demonstrated better capability for reproducing HCHO distribution in N-Africa (r = 0.65). Negative model bias in N-Africa is

almost half (22%) that of S-Africa (46%). Observed N-African HCHO columns are mostly higher than 1.2×10^{16} molecules cm^{-2} during the biomass burning period (November - April). Although the modeled values are lower than the observed values, the year-end columns (November - December) are similar. Both datasets show low HCHO variation during May - September. Over the S-African region, the model capabilities were limited.

Over S-America, the negative bias (~22%) in the model estimates compared to the observations is similar to that of N-Africa. In addition to consistency in the year-end (November to December) columns, CHASER well reproduced the biomass burning-led enhancements. The observed and simulated magnitudes of seasonal modulation are 49 and 43%, respectively.

Over SE-Asia, CHASER reproduced the observed biomass burning-led enhanced HCHO columns during the dry season (January - April), however, the occurrence of the peak is inconsistent. As discussed in section 3.1, observed HCHO peaks related to biomass burning can vary depending on the fire numbers. The *r*-value (0.48) is moderate and model is biased by 30% in the lower side. The model negative biases in the biomass prone regions are lowest (<30%) among the discussed regions.

From results of a recent study, De Smedt et al. (2021) reported that, cloud corrections can positively bias OMI HCHO columns up to 30% compared to Tropospheric Ozone Monitoring Instrument (TROPOMI) columns. Consequently, uncertainties in the observations are also likely to contribute to the observed negative biases. Comparison among CHASER, TROPOMI, and OMI HCHO columns is beyond the scope of this study. However, the effects of uncertainties in the satellite retrievals on the negative biases is discussed qualitatively and briefly. To demonstrate such effects, CHASER and TROPOMI HCHO columns for 2019 are compared in Fig S3. The simulation settings and emission inventories are similar to those explained in section 3.2.3. The comparison results are presented in Table S2. TROPOMI data has been processed following De Smedt et al. (2021). The CHASER and TROPOMI HCHO spatial distribution correlates strongly with *r*-value of 0.78. The values for MBE and RMSE are respectively, -2.3×10^{15} and 2.8×10^{15} molecules cm^{-2}. Compared to OMI and TROPOMI, CHASER HCHO columns are negatively biased, respectively, by 61 and 38%. The model biases are lower when compared to TROPOMI observations. Because of temporal differences in the two comparisons, the biases cannot be

compared quantitatively. However, the differences in the biases signify that the observational uncertainties can strongly affect discrepancies between the simulated and observed HCHO abundances.

3.3 Evaluation of CHASER simulations at the three sites

3.3.1 Evaluation of CHASER HCHO at Phimai and Chiba

The seasonally averaged observed and modeled HCHO profiles and partial columns in the 0 - 4 km altitude range at Phimai and Chiba are presented in Fig. 10. The CHASER outputs smoothed with MAX-DOAS averaging kernels (AK) are also depicted. The AK is applied following Franco et al. (2015). First, the CHASER HCHO profiles are interpolated to the MAX-DOAS vertical grids. Next, the MAX-DOAS AK information from individual retrieved profiles is seasonally averaged according to the climate classifications of each site. Finally, the CHASER outputs on the coincident days are selected, and the seasonally averaged AK is applied to the daily mean interpolated profile. Applying individual AKs to the model outputs yielded similar results. The seasonally averaged AKs for both sites are shown in Fig S4. The coincident days at Phimai and Chiba were respectively,690 and 668.

At Phimai, CHASER predicted the increase in the HCHO partial columns during the dry season and well-reproduced the HCHO seasonality. The simulated and observed seasonality correlates strongly with *R*-value of 0.96. The modeled monthly mean values during the dry season are found to be within the 1σ standard deviation of the observed values, indicating that the pyrogenic emissions estimates used for the simulations are reasonable. CHASER predicted a 41% increase in the HCHO column during January - March, consistent with the observations (41%). CHASER overestimates the HCHO columns in both seasons, and the mean bias error (MBE) (CHASER – MAX-DOAS) is lower (3.7×10^{15} molecules cm^{-2}) (Table 6) during the wet season. Although underestimated, the dry season smoothed column values are within the 1σ range.

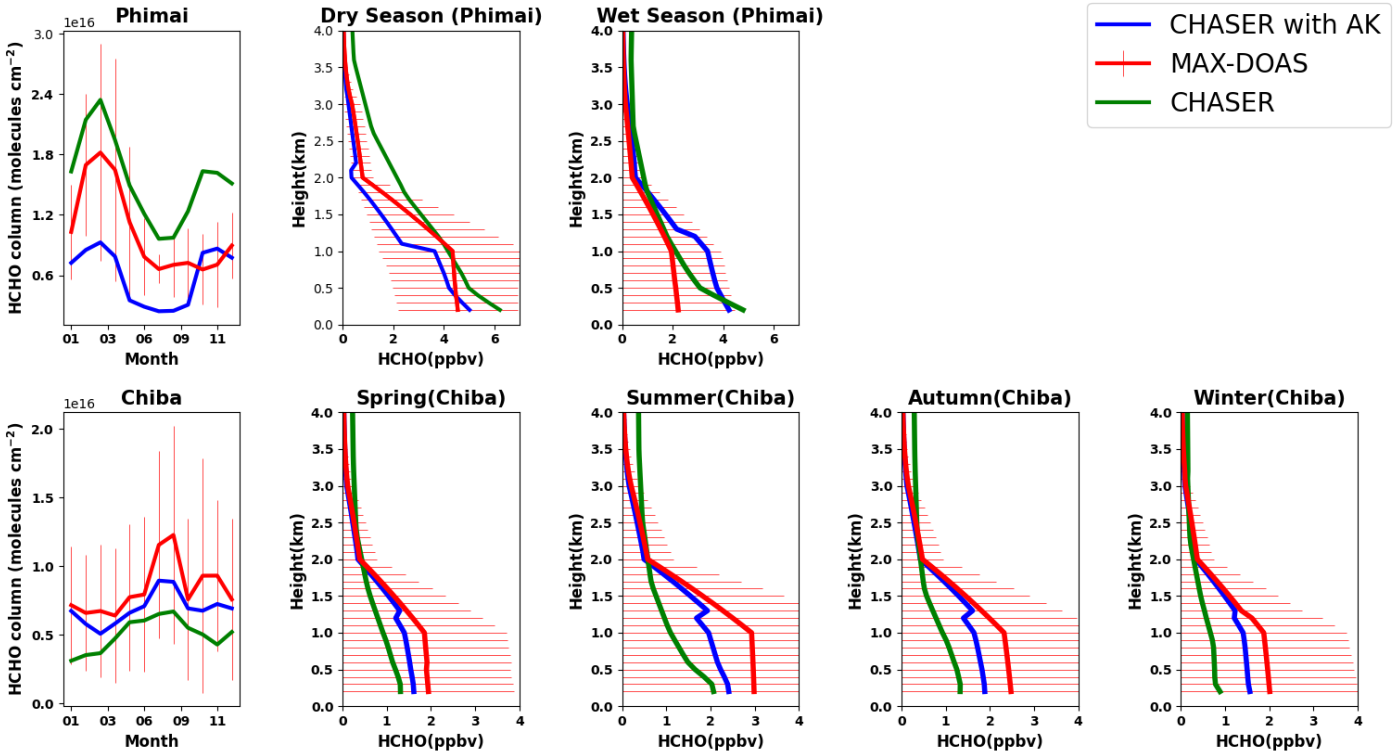

744 **Figure 10.** Seasonal variations in the HCHO partial columns at 0 - 4 km and vertical profiles during all seasons at
745 Phimai and Chiba, as inferred from the MAX-DOAS observations (red) and CHASER simulation(green). The
746 CHASER HCHO partial column and vertical profile smoothed with the MAX-DOAS AK are coloured blue. The
747 AK information of all the screened (as explained in section 2.2) retrievals were averaged based on the seasonal
748 classification of the respective sites. The coincident time and date between the model and observations are selected
749 only. Error bars indicate the one sigma standard deviation of mean values of the MAX-DOAS observations.
750
751 The modeled and observed HCHO mixing ratios in the 1- 2km layers during the wet season are almost
752 identical, whereas VMR near the surface (i.e., 0 - 1 km) differ by 30%. The absolute mean difference in
753 the 0-4 km layer is ~0.45ppbv, with the maximum difference of 2.58 ppbv below 200 m. CHASER has
754 demonstrated good capabilities for reproducing the HCHO profile in the 0.5 – 4 km layer during the wet
755 season. The significance of AK information is low for the wet season. However, smoothing the model
756 profiles reduces the overall MBE by 43%.
757

Table 6: Comparison of the seasonal mean HCHO partial columns and profiles (0-4 km) between MAX-DOAS and CHASER at Phimai and Chiba. MBE (CHASER – MAX-DOAS) is the mean bias error. The partial column and profile MBE units are respectively, $\times 10^{16}$ molecules cm^{-2} and ppbv, respectively.

Site	Season	Partial column MBE	Smoothed Partial column MBE	Profile MBE	Smoothed Profile MBE
Phimai	Overall	0.28	-0.07	0.35	0.01
Phimai	Dry	0.37	-0.28	0.58	-0.38
Phimai	Wet	0.21	0.07	0.45	0.33
Chiba	Overall	-0.12	-0.05	-0.37	-0.11
Chiba	Spring	-0.07	-0.04	-0.22	-0.12
Chiba	Summer	-0.16	-0.08	-0.45	-0.26
Chiba	Autumn	-0.10	-0.04	-0.40	-0.19
Chiba	Winter	-0.09	-0.01	-0.42	0.11

During the dry season, the respective absolute mean and maximum difference in the datasets in the 0 -1 km layers is ~1 and ~2ppbv. The observed and simulated seasonal differences in the 0-1 km are 50 and 34%, respectively. Simulated dry season profile values at the heights greater than ~2 km are out of the 1σ variation range. The two-potential reasons for such differences are lower measurement sensitivity in the free troposphere and the overestimated Southeast Asian biogenic emissions in the model. Despite the measurement limitations, CHASER and MAX-DOAS wet season profiles up to 3 km are consistent. Consequently, it is likely that the biogenic emissions for this region in the model are overestimated. The Southeast Asian isoprene emissions in CHASER is 128 $Tgyr^{-1}$, higher than the CMAS-GLO-BIO (Sindelarova et al., 2022) inventory (78 Tgyr-1). However, the dry season HCHO profiles in 0 - 2 km are well simulated. Smoothing underestimates the dry season profile within the 1σ variation range but improved simulations below 200 m. At heights greater than 3 km, the smoothed values mostly reproduce the a priori because of reduced measurement sensitivity (i.e., low AK value, indicating limited information was retrievable).

Moderate correlation (R=0.58) can be observed between the modeled and observed HCHO partial columns at Chiba. CHASER was able to reproduce the peak in the partial columns in August. The model predicts a 41% increase in the HCHO columns during January - August, whereas the observed increase is 54%. Although Chiba is an urban site, the HCHO and temperature seasonal variations show a tight correlation (R~ 0.70) (Fig S5), suggesting that changes in biogenic emissions modulate HCHO seasonality. Similarly, the modeled seasonality is consistent with temperature variation (Fig. S4). Thus, the simulated HCHO seasonality in Chiba is reasonable, despite underestimation of absolute values. Smoothing the simulations improve the correlation, and the MBE is reduced by 54% (Table 6).

The CHASER HCHO profiles in the 0 - 4 km layers are lower than the observations, with an MBE of 0.39 ppbv. The absolute differences in the modeled and retrieved HCHO profiles in the 0-2 km layer during all seasons are higher than at Phimai. Absolute mean differences of ~ 1pbbv and higher are mainly observed for 0 to 2 km. In addition, the vertical gradients of the simulated profiles are low compared to those at Phimai. The modeled profiles at Chiba resemble the HCHO profiles measured over the ocean during the INTEX-B (Intercontinental Chemical Transport Experiment: Phase B) (Boeke et al., 2011). The Chiba site is near the sea, and coarse CHASER resolution includes the ocean pixels. Moreover, urban surfaces are not homogeneous. Thus, a significant part of the profile discrepancies is likely related to the systematic differences, in addition to emission estimates. However, the model estimates lie within the standard deviation range of the measurements. Because of the low gradients in the simulated profiles, the smoothed profiles mostly imitated the a priori values even below 2 km. Overall, the differences between the observations and smoothed profile are statistically insignificant. Effects of the horizontal resolution on the simulated HCHO levels is discussed in section 3.3.4.

3.3.2 Evaluation of CHASER NO_2 in Phimai and Chiba

Figure 11 presents the seasonal averages of the MAX-DOAS and CHASER NO_2 profiles and partial columns (0 - 4 km) at Phimai and Chiba. The AK is applied to the modeled outputs for the Chiba site only.

Figure S5 of the supplementary information presents a comparison of the observations, model, and smoothed model profiles averaged within the 0 - 2 km layer at Phimai. Smoothing with different a priori values is depicted to demonstrate the effects of the a priori values. The smoothed NO_2 concentrations, calculated using the original a priori values, show a seasonal variation shift. The mean smoothed profile resembles the observations when a priori values are reduced by 50%; however, the dry season values are similar in both cases. Two test cases of smoothing profiles using apriori values above 500 and 800 m shows good agreement with the observations; however, the results are sensitive to the apriori values. Because smoothed profiles are strongly biased to the apriori choice, the smoothing results obtained for the Phimai site are discarded.

The modeled NO_2 partial column at Phimai shows good agreement with observations made during the dry season. CHASER well reproduces the enhanced NO_2 columns attributable to biomass burning within the standard deviation of the observations. The peak in the NO_2 levels during March is consistent in both datasets. Although the seasonality does not agree in other months, the overall MBE is 8×10^{13} molecule cm^{-2} (Table 7). Above 500 m, the datasets shows excellent agreement. The absolute mean differences in the 0 - 1km layer are 0.22 ppbv, and the maximum difference of ~1.9 ppbv is observed near the surface. Amidst the biomass burning influence, the NO_2 concentrations at Phimai are mostly < 1 ppbv. Thus, the results of comparisons demonstrate CHASER's good capabilities in regions characterized by low NO_2 concentrations. Moreover, when NO_2 concentrations are less than < 1 ppbv, the AK information seems less significant if the model can capture low-concentration scenarios.

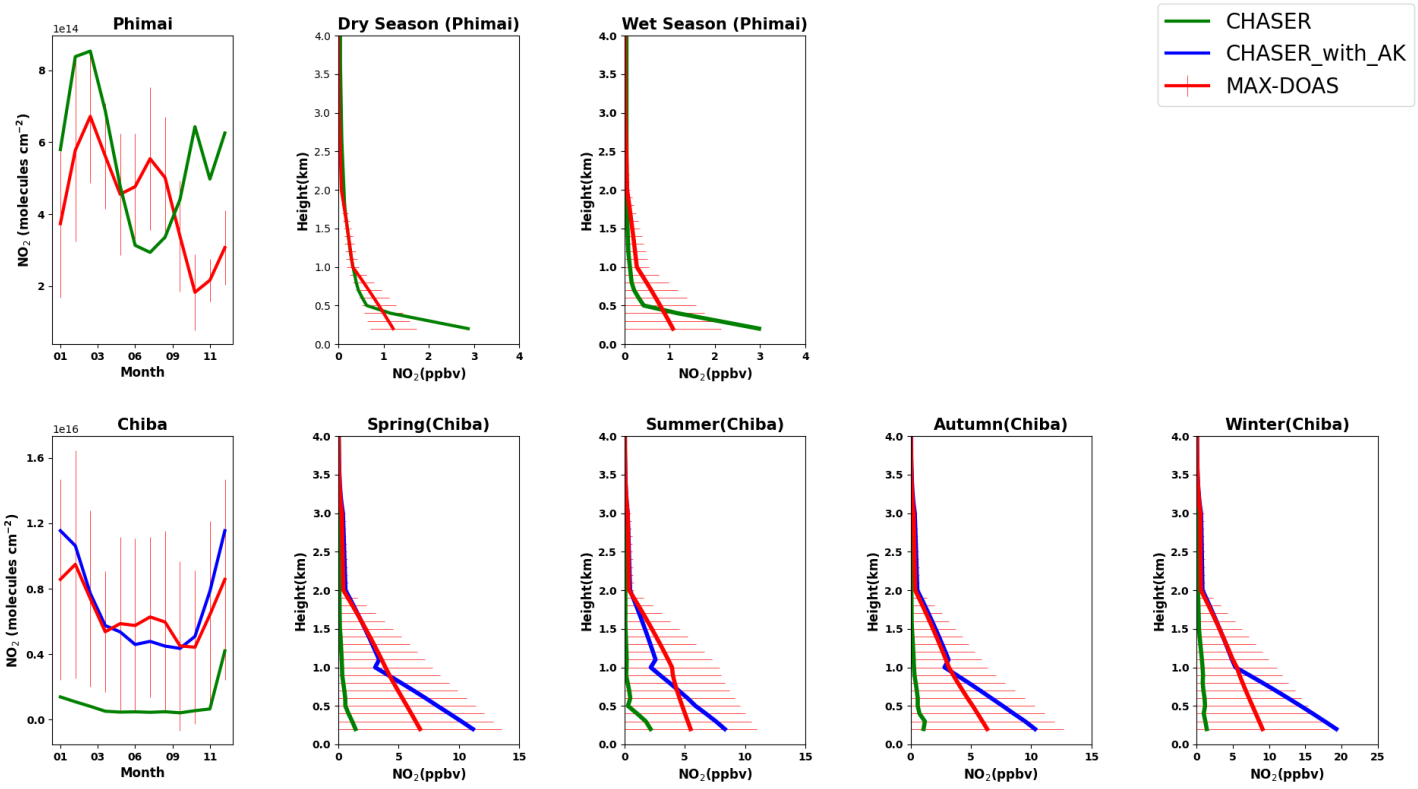

Figure 11. Seasonal variation in NO_2 partial columns from 0 - 4 km and vertical profiles during all seasons at Phimai and Chiba, as inferred from the MAX-DOAS observations (red) and CHASER simulation(green). The CHASER NO_2 partial column and vertical profile smoothed with the MAX-DOAS AK are coloured in blue. The coincident time and date between the model and observations are selected only. The error bars represent the one sigma standard deviation of mean values of the MAX-DOAS observations.

Table 7: Comparison of the seasonal mean NO_2 partial columns and profiles (0-4 km) between MAX-DOAS and CHASER at Phimai and Chiba. MBE (CHASER – MAX-DOAS) is the mean bias error. The partial column and profile MBE units are $\times 10^{15}$ molecules cm^{-2} and ppbv, respectively.

Site	Season	Partial column MBE	Smoothed Partial column MBE	Profile MBE	Smoothed Profile MBE
Phimai	Overall	0.08		0.11	
Phimai	Dry	0.18		0.09	
Phimai	Wet	-0.14		0.02	
Chiba	Overall	-5.58	-1.90	-3.27	-1.66
Chiba	Spring	-5.56	-2.00	-3.19	-1.74
Chiba	Summer	-5.52	-2.87	-2.85	-1.86
Chiba	Autumn	-4.57	-1.24	-2.74	-1.40
Chiba	Winter	-6.64	-1.50	-4.30	-1.63

Although the datasets are moderately correlated (R=0.59) at Chiba, the model largely underestimates the NO_2 partial column with MBE of ~5×10^{15} molecules cm^{-2}. The model predicts almost constant NO_2 profiles and columns throughout the year. Therefore, the respective seasonal biases are almost similar. The vertical gradient of the modeled NO_2 profiles is also low, too, similarly to the HCHO profiles. The model resolution can be a potential cause for such significant underestimation. The AKs improved the partial column and profiles significantly, reducing the MBE by more than 50%. However, the smoothed profiles and partial columns between the 0 - 2 km layer, differ significantly from the simulations, suggesting that the a priori values strongly affect the smoothed profiles. Consequently, the smoothed NO_2 profiles at Chiba (Fig. S5) are biased to the a priori values, similarly to that of at Phimai (Fig. S5). NO_2 smoothed profile sensitivity to a priori values might be attributable to our retrieval procedure. The a priori data are taken from the measured SCD and retrieved VCD values. As a result, the values are sensitive in the 0 - 2 km layer, similarly to the observations. Using a priori values other than those obtained from observations can affect such sensitivity. The smoothing sensitivity to a priori values is stronger for NO_2 than HCHO. The NO_2 profile gradient is higher than that of HCHO (Figs. 10 and 11), which means that,

854 within 10 km (MAX-DOAS horizontal resolution), the NO_2 mixing ratio and a priori variability (sources
855 and sinks) is higher than those of HCHO, leading to a stronger a priori effect on the smoothed profiles.
856
857 The mean NO_2 mixing ratios in the 0 - 2 km layer in 2018, simulated at spatial resolutions of 2.8˚ × 2.8˚
858 (standard) and 1.4˚ × 1.4˚, are compared with observations at Chiba, as depicted in Fig.12. The error bars
859 are the 1σ standard deviation of the observations. Higher resolution simulations reduced the overall MBE
860 by 35% (Table 8). NO_2 concentrations at 1.4˚ are now within the variation range of the observations. The
861 1.4˚ simulation captured the NO_2 seasonal variability better than at 2.8˚. Despite improved resolution, the
862 model values are underestimated, with the highest MBE during the winter. According to Miyazaki et al.
863 (2020), the seasonality in the anthropogenic emissions, primarily wintertime heating, is not well
864 represented in the emission inventories, which could likely underestimate winter NO_2 levels. The best
865 agreement between the datasets is observed during summer and spring, with an MBE of ~1 ppbv on a
866 seasonal scale.
867

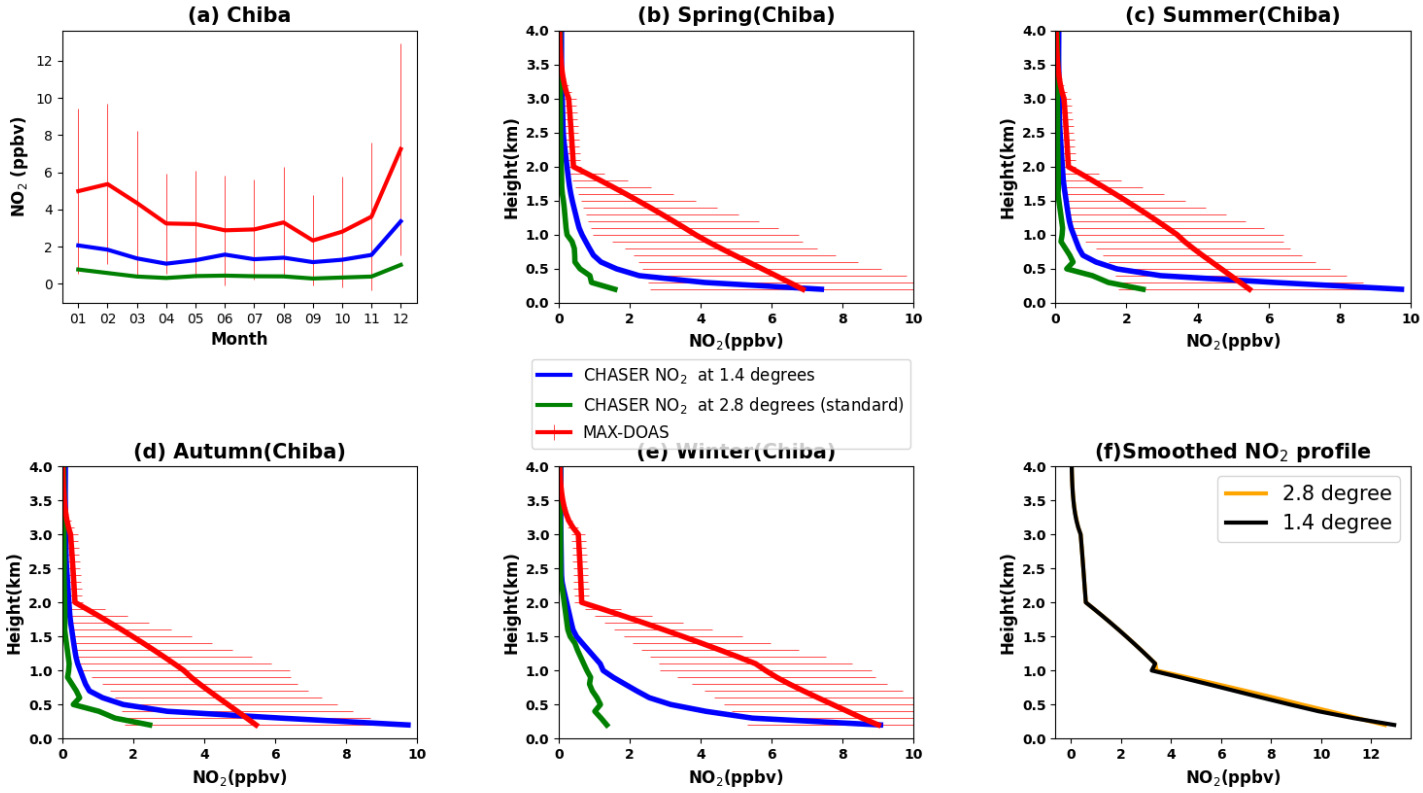

868 **Figure 12**: (a) Seasonal variations in the NO_2 mixing ratios in the 0 - 2 km layer at Chiba, as inferred from the
869 MAX-DOAS observations (red) and two CHASER simulations at 2.8˚(green) and 1.4˚(blue) resolutions. The
870 simulated NO_2 profiles at 2.8˚(green) and 1.4˚(blue) resolutions during (b) spring, (c) summer, (d) autumn, and (e)
871 winter are shown with the observed seasonal profiles at Chiba. Only data (both observed and simulated) for 2018
872 are plotted. The coincident time and date between the model and observations are selected only. The error bars in
873 (a), (b), (c), and (d) represent the one sigma standard deviation of mean values of the MAX-DOAS observations.
874
875
876 NO_2 profiles at 2.8˚ and 1.4˚ resolution are shown in Figs. 12(b - e). A strong effect of the increased
877 resolution is observed below 500 m, reducing the negative bias by 70% near the surface. Above 500 m,
878 the effects of higher resolution are limited, with an MBE reduction of 12% in the 0.6 – 2 km. Although
879 the near-surface NO_2 concentrations at 1.4˚ resolution are overestimated, the values are within the
880 standard deviation of the observations. At around 200m, winter mean NO_2 concentrations at 1.4˚

resolution are identical to the observations (~9 ppbv), and the summer mean is overestimated. Moreover, the NO_2 levels above 2 km are similar at both resolutions. The resolution effects on NO_2 profiles vary with the location and season (Williams et al., 2017). For example, CHASER NO_2 at 1.1˚ resolution improved the agreement with aircraft observations below 650 hPa significantly over the Denver metropolitan area (Sekiya et al. 2018), whereas, at Chiba, the 1.4˚ resolution improved the surface estimates. Consequently, the horizontal resolution is not the only reason for the model underestimation. Other factors such as the vertical resolution, uncertainties in emission inventories, and chemical kinetics, can also affect the simulated NO_2 estimates. Effects of the emission inventory is discussed in section 3.3.4.

Figure 12(f) shows the smoothed NO_2 profiles at both resolutions. Although the profile shapes are different, the smoothed profiles are almost identical, which demonstrates that, smoothed NO_2 profile sensitivity to a priori choice is mostly independent of the model resolution.

Table 8: Comparison of the seasonal mean NO_2profiles (0-2 km) among MAX-DOAS and CHASER simulations at 2.8˚ and 1.4˚ resolutions at Chiba. MBE at (CHASER – MAX-DOAS) 1.4˚ and 2.8˚ are the mean bias error at the respective resolutions. The MBE unit is ppbv.

Season	**MBE at 1.4˚**	**MBE at 2.8˚**
Overall	-2.24	-3.37
Spring	-2.26	-3.23
Summer	-1.50	-2.47
Autumn	-1.57	-2.57
Winter	-3.44	-5.07

3.3.3 Evaluation of CHASER HCHO in the IGP region

The IGP is the most fertile region in South Asia, which accounts for approximately 50% of the total agricultural production of India and is one of the significant contributing regions to the global greening based on leaf area index (Sarmah et al., 2021). Moreover, IGP is one of the regional HCHO hotspots in India (Chutia et al., 2019). The observed HCHO seasonality at Pantnagar is consistent with that reported by Mahajan et al. (2015) for the entire IGP region. Consequently, comparison with the HCHO retrievals in Pantnagar can assess the model capability in the IGP region. The spatial representativeness is a limitation for comparison between a point measurement and regional simulations. Thus, the results are interpreted qualitatively. Because of the availability of a dataset with continuous observatios, only the comparison for 2017 is shown in Fig. 13.

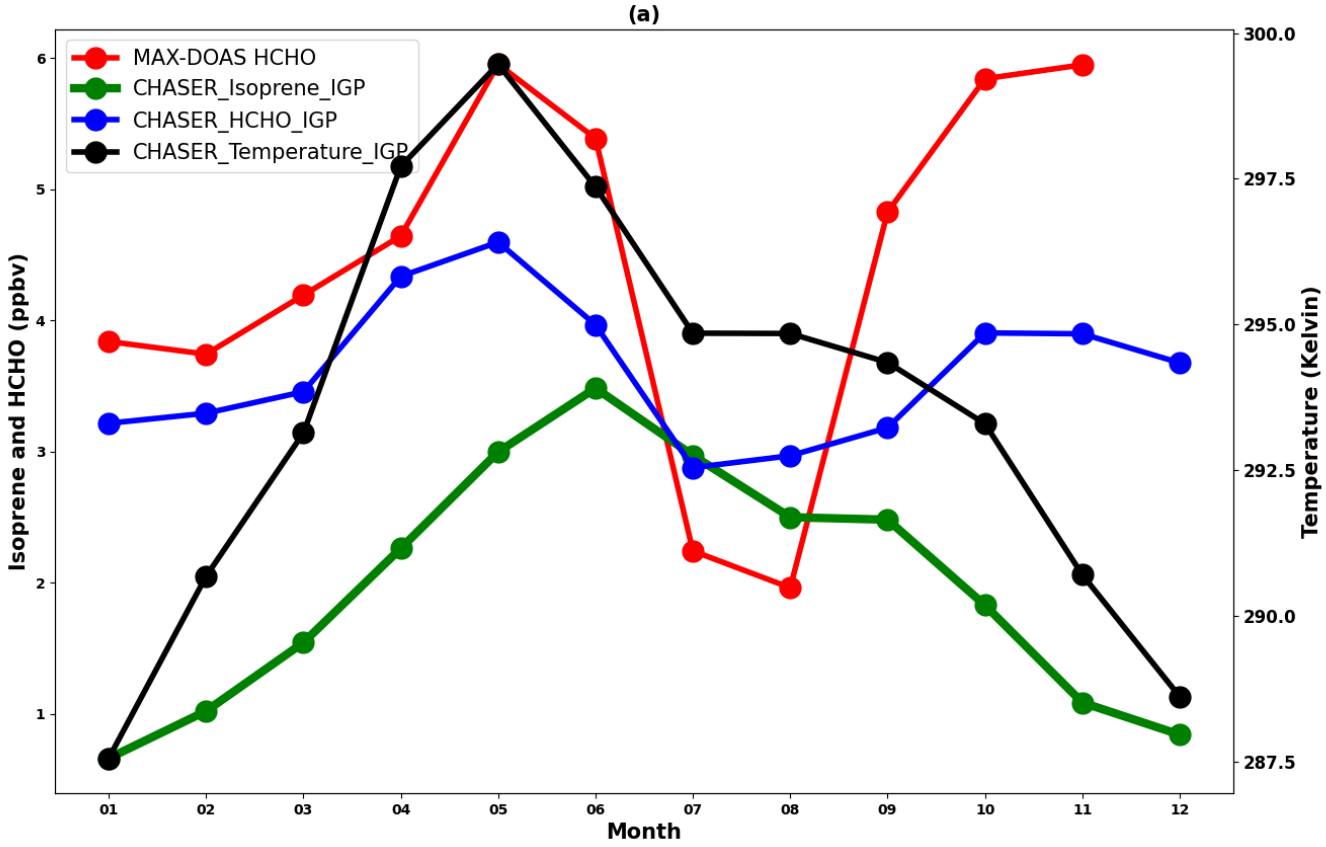

Figure 13. Seasonal variations in the MAX-DOAS (red) and CHASER (blue) HCHO concentrations at Pantnagar and the IGP region, respectively, in 2017. The coincident dates between the observations and model are plotted

only. The CHASER simulated isoprene and temperature seasonality are shown respectively, in green and black colours. Only the daytime simulated values were considered for the plot.

The modeled HCHO seasonal variations in the IGP region correlate well with the observations at Pantnagar (R~ 0.80). The enhancement in the HCHO concentrations during the spring and post-monsoon season is well reproduced by CHASER, which indicates that CHASER can capture HCHO variation in complex terrain region such as IGP. Figure 13 also depicts the isoprene concentrations and temperature in the IGP region, in addition to the HCHO concentrations. Oxidization of precursor hydrocarbons and photochemical reactions are the most dominant sources of HCHO. Also, isoprene is the most abundant hydrocarbon in the atmosphere. The average ambient isoprene concentrations during July, August, and September in the IGP region are 1.4 ± 0.3 ppbv (Mishra et al., 2020). Therefore, the CHASER isoprene concentration range of 1.5 – 2 ppbv during the monsoon season seems reasonable. The HCHO concentrations in the IGP region reach a peak during the spring and post-monsoon seasons. A strong correlation between HCHO, isoprene, and temperature variation (R ~ 0.90) during the first half of the year indicates that the change in biogenic emissions strongly drives the HCHO seasonal modulation. The observed enhancement in the HCHO levels during spring at Pantnagar is related to biomass burning. The biomass burning events are primarily concentrated in the northwest IGP region (Kumar and Sinha, 2021), where the site is located. On a regional scale, the biomass burning effects is expected to smear. Thus, the strong effect of the biogenic emission on the regional HCHO modulation is reasonable. HCHO modulation differs from isoprene and temperature during the post-monsoon period, suggesting a greater role of biomass burning and anthropogenic emissions. Consequently, the physical processes driving the HCHO seasonality in the IGP region are well reflected in the CHASER simulations.

3.3.4 Effects of the model resolution and emission inventories on results

Effects of the spatial resolution on the evaluation results is assessed by comparing the results of CHASER simulations at 2.8˚ and 1.4˚ resolutions with the surface observations, as shown in Fig. 14. Only, the simulated surface HCHO and NO_2 concentrations during 2017 are shown only. The statistics are provided in Table 9. For the Pantnagar site, only the simulations are presented. At Phimai, the HCHO simulations

differ by 3%. The standard simulation shows better agreement with the observations. The higher MBE at 1.4˚ occurred mostly because of the model overestimation during the wet season. The NO_2 mixing ratios at the two resolution differ by 9%. The MBEs for both trace gases at Phimai are less than 1 ppbv. Thus, the HCHO and NO_2 standard simulations at 2.8˚ can be regarded as reasonable for regions characterized by low NO_2 levels (<1 ppbv). At Chiba, surface NO_2 and HCHO mixing ratios at 1.4˚ resolution differ respectively, by 61 and 19%. The NO_2 MBE at 1.4˚ resolution improved significantly, indicating a strong effect of the model resolution. However, discussion in section 3.2.2 showed limited resolution-based improvement in the overall profile. Results for MBE in the HCHO mixing ratios at 1.4˚ mostly improved during summer. The wintertime HCHO estimates at both resolutions are similar. In contrast to Chiba and Phimai, differences in the HCHO simulations (30%) at Pantnagar are greater than those of NO_2 (3%). The effect of model resolution varying with location and season was also reported by Sekiya et al. (2018). Compared to the other two sites, differences in the NO_2 simulations at Chiba are larger. This finding is consistent with the results by William et al (2017), which found larger differences with changing model resolution over urban areas.

Although the NO_x estimates for the low NO_2 regions seem reasonable, global NO_x emissions have changed since 2008(i.e., EDGAR-HTAP (2008) emissions used for this study). A recent study by Miyazaki et al. (2020) reported changes in global NO_x emissions from 2005 to 2018. They found a continuous 30% increase in NO_x emissions in India since 2005. REAS v3 (Regional Emission inventory in Asia version 3) inventory estimated a 23% increase in NO_x emissions in India between 2010 - 2015, and power plants were the most significant contributor. Many power plants are clustered along the IGP region (Nair et al., 2007). Thus, the current simulation settings are likely to underestimate the NO_2 mixing ratios and columns in the IGP region. Figure S7 presents comparison of CHASER and OMI NO_2 columns for 2017 over the IGP region. Although the modeled columns are biased by 32% in the lower side, the spatial correlation between the datasets is high (r=0.78). CHASER values lie within the range of variation of the observations. Although underestimated, NO_2 estimates in the IGP based on the current inventory are yet reasonable. Sekiya et al., (2018) used higher model resolution and updated emission inventory (HTAP 2010 for simulations in 2014) and reported ~30% lower MBE over India. However, the RMSE values of both studies are comparable.

NO_x emissions in Japan have shown continuous decline since the execution of pollution control policies in 1970 (Ohara et al., 2020). Irie et al. (2021) reported a declining trend in NO_2 levels in Chiba since 2012, echoing results obtained by Miyazaki et al. (2020) throughout Japan. The bias between CHASER and OMI NO_2 column over Japan is non-significant (Fig. S7 and Table S3). Thus, an updated inventory will not substantially affect the comparison results at the Chiba site. NO_x emissions increased considerably in Southeast Asia. CHASER NO_2 estimates for Thailand based on HTAP 2008 inventory are biased by 45% in the lower side compared to OMI (Fig. S7). However, Phimai being a rural site, the NO_x levels are expected to be low. Changes in biomass burning NO_x estimates are likely to affect the model estimates. Because, the NO_2 levels at Phimai are mostly less than 1 ppbv, the effect of updated inventory on the comparison results is expected to be minimal.

CHASER HCHO columns over Japan, the IGP region, and Thailand are negatively biased respectively, by 60, 36, and 32% compared to OMI observations, with *r*-values of 0.5 – 0.7 (Fig. S7). Surl et al. (2018) reported spatial correlation of ~0.5 between GEOS-CHEM and OMI over the IGP region. Anthropogenic VOC emissions in India and other Asian cities have increased since 2005, whereas a negative trend has been observed over Japan (Bauwens et al., 2022). The REAS inventory estimated a 5% increase in NMVOCS in India since 2005. Moreover, anthropogenic emission contributes strongly to the HCHO abundances in the IGP region (Kumar and Sinha 2021). Thus, updated anthropogenic VOC emission inventory is likely to improve the model HCHO estimates in the study regions. However, the formation pathway of HCHO from isoprene emissions is a non-linear function of NO_x chemistry. Consequently, the effects of NO_x emissions changes on the overall HCHO simulations cannot be assessed based on current analyses explained herein.

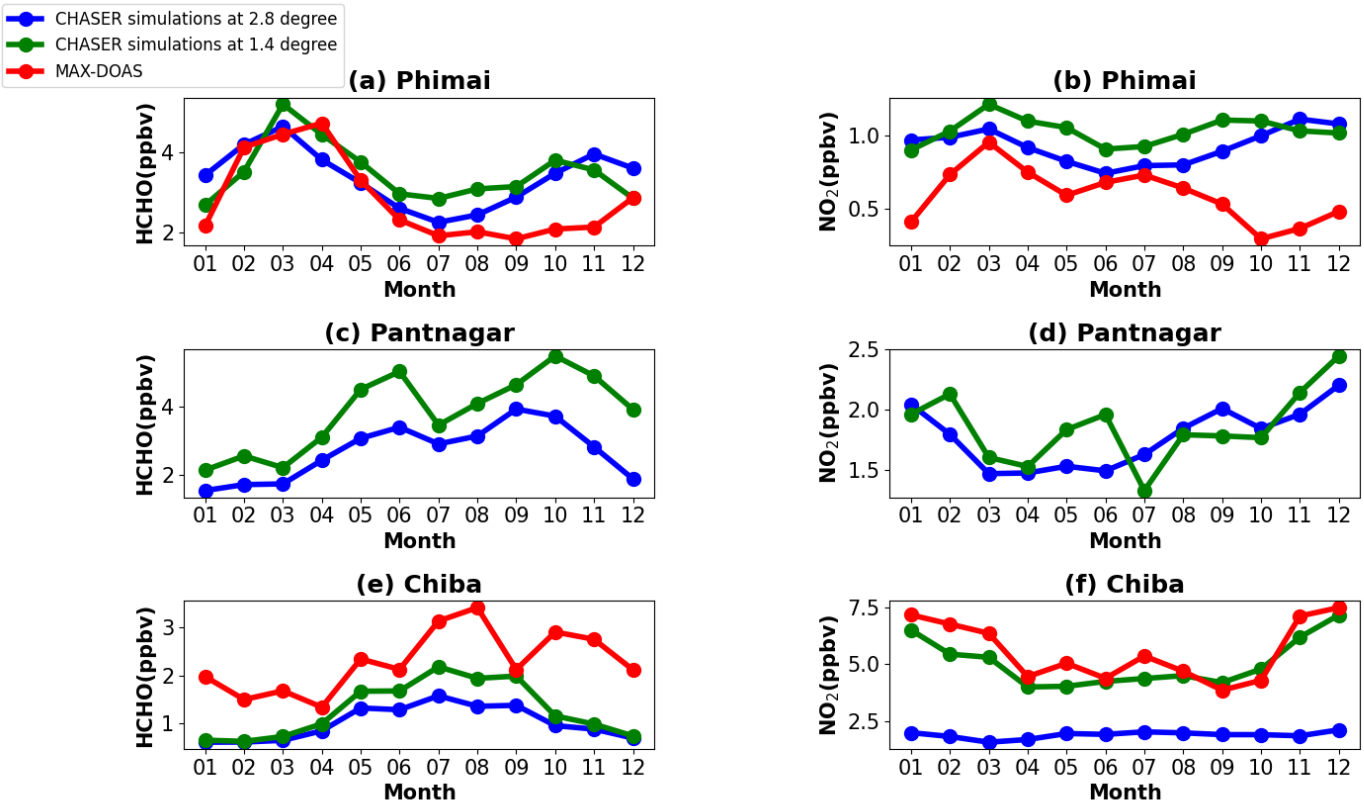

Figure 14. Seasonal variation in the surface HCHO and NO_2 mixing ratios at (a & b) Phimai, (c & d) Pantnagar, and (e & f) Chiba simulated at spatial resolutions of 2.8˚ ×2.8˚ (blue) and 1.4˚ × 1.4˚(green). Coincident MAX-DOAS NO_2 and HCHO VMRs in the 0-1 km layer at Phimai and Chiba are plotted in red. Observation at Pantnagar are discarded. Only the datasets for 2017 are plotted.

Table 9: The comparison between the observations and simulations at 2.8˚ and 1.4˚ spatial resolutions. The MBE is the mean bias error. The unit of MBE is ppbv.

Site	Trace gas	MBE at 2.8˚	MBE at 1.4˚	Differences between the simulations
Phimai	HCHO	0.54	0. 65	3%
Phimai	NO_2	0.33	0.43	9%
Chiba	HCHO	-1.27	-1.00	19%
Chiba	NO_2	-0.52	-3.69	61%
Pantnagar				30%
Pantnagar				3%

3.4 Contribution estimates

3.4.1 Contribution from biomass burning to the HCHO and NO_2 abundances at Phimai

Good agreement between the datasets in the 0 - 1 km layer at Phimai can quantify biomass burning contributions to the HCHO and NO_2 concentrations. Figure 15 presents results of simulations L1_HCHO, L1_opt, and L1_NO_2. The simulation settings are presented in Table 3. For better readability, the switched-off emissions criterion is described in the legends of Fig.15. The plots present mean mixing ratios in the 0 – 1 km layer. Biomass burning contributes ~10% to the HCHO concentrations at Phimai during the dry season. However, based on the observations, a greater effect of biomass burning is expected. During the wet season, the MAX-DOAS and CHASER HCHO surface mixing ratios are, respectively, ~2 and ~4 ppbv (Fig. 10), indicating overestimation of the biogenic emissions in CHASER. Figure 15(b) shows the HCHO concentration obtained from simulation L1_opt and MAX-DOAS observations in 2017. In the L1_opt simulation setting, the biomass burning emissions are switched off;

the biogenic emissions are optimized to reproduce results analogous to those obtained from observations during the wet season. In the absence of biomass burning, the surface HCHO concentrations at Phimai would be ~2 ppbv, indicating a biomass burning contribution of ~20–50% during the dry season. The observed interseason difference in the HCHO concentration at Phimai is ~60%. Consequently, the revised biomass burning contribution estimate is more reasonable. Pyrogenic emissions contributions to the NO_2 concentrations at Phimai are ~10% during the dry season (Fig. 15(c)). Because the NO_2 concentrations are low at Phimai, the simulation results obtained for March, when the influence of biomass burning is highest, are used to derive a better contribution estimate. In the absence of biomass burning, the NO_2 concentration during March would be about 0.84 ppbv (Fig.15(d)), indicating a contribution as high as 35% to the NO_2 concentrations at Phimai.

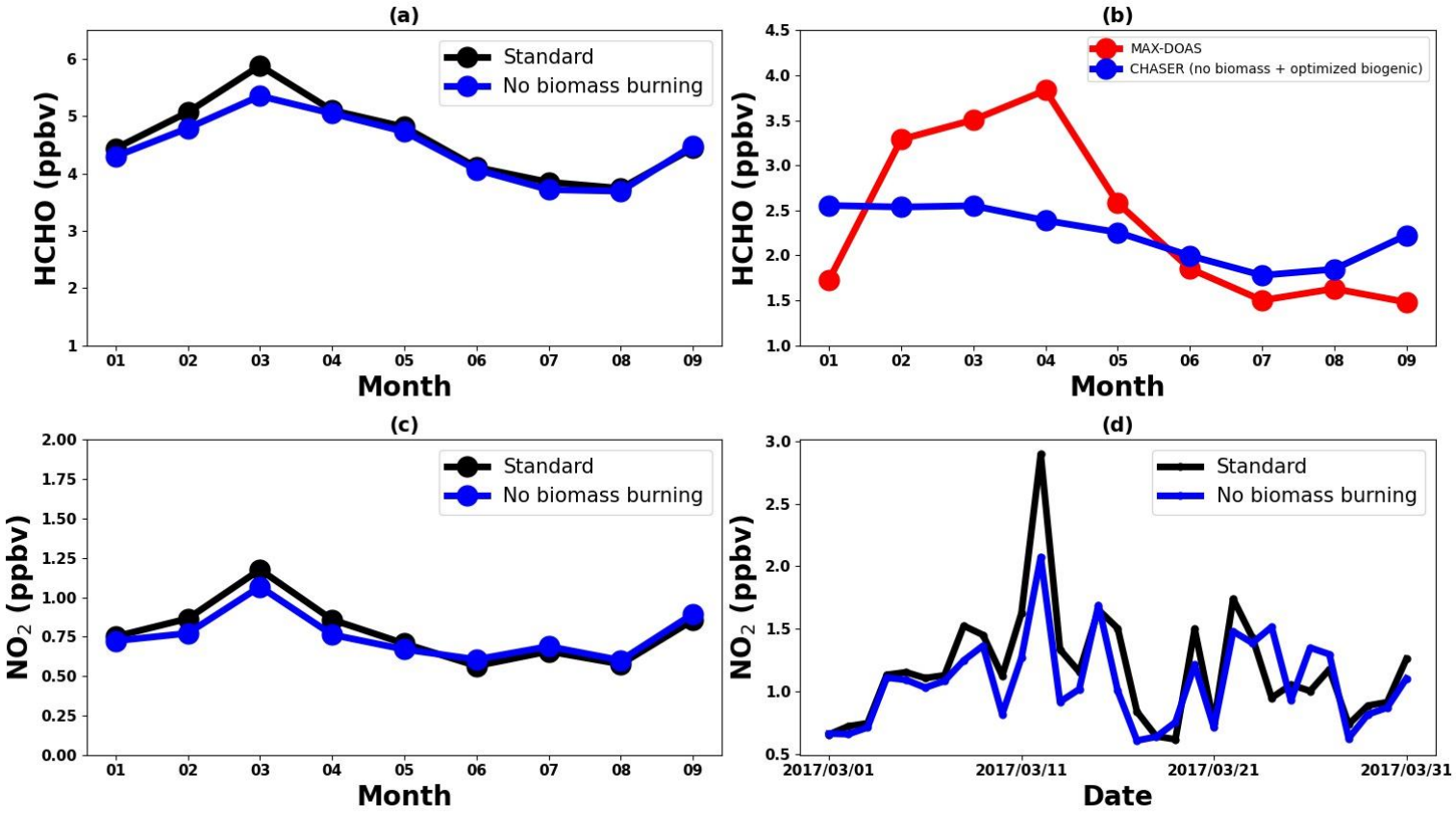

Figure 15. (top panel) (a) Seasonal variations in the HCHO concentrations in the 0 - 1 km layer at Phimai, as obtained from the standard and L1_HCHO simulations. Pyrogenic emissions of VOCs are switched off in L1_HCHO. (b) The HCHO seasonal variation in Phimai in 2017, as obtained from the MAX-DOAS observations (red) and L1_opt simulations. The pyrogenic VOC emissions were switched off, and the biogenic emissions were reduced by 50% in L1_opt. The coincident dates between the observation and the simulations are shown only. (bottom panel) (c) Seasonal variations in the NO_2 surface concentrations at Phimai in 2017, as obtained from the standard and L1_NO_2 simulations. (d) Standard and L1_NO_2 simulation outputs of the daily mean NO_2 surface concentrations during March 2017. The pyrogenic NO_2 emissions were switched off in the L1_NO_2 simulation. Only the daytime values from 09:00 – 15:00 LT are used to calculate the seasonal mean.

3.4.2 Contribution of soil NO_x emissions at Phimai

Because soil NO_x emissions are included in CHASER simulations, the NO_2 contributions from soil emissions are quantified. Figure 16 presents the monthly mean surface NO_2 concentrations at Phimai in 2017, simulated including (standard) and switching off (L1_NO_2) the soil NO_x emissions. The NO_2 concentrations between 09 and 12 hr. were used to calculate the monthly mean concentrations. Soil emissions contribute ~20% of the overall NO_2 concentrations at Phimai, with higher contributions during the wet season. The highest soil contribution of about 25% occurs in July.

3.4.3 Contribution from pyrogenic and anthropogenic emissions to the HCHO abundances in the IGP region

Figure 16(b) presents the standard, L1_HCHO (pyrogenic VOC emissions switched off), and L2 (anthropogenic VOC emissions switched off) HCHO simulations in the IGP region. According to L1_HCHO simulation results, effects of biomass burning emissions on the regional HCHO modulation are small (~12%). The HCHO concentrations in India have biogenic, anthropogenic, and pyrogenic VOC sources. However, biogenic VOCs are the primary driver of the over HCHO variation (Surl et al., 2018). Consequently, two reasons might be responsible for the small effects of pyrogenic emissions on HCHO concentrations: (1) Overestimation of the biogenic emission or underestimation of pyrogenic emissions in the model. (2) Stronger effects of anthropogenic VOC emissions than of pyrogenic VOCs. The L2

simulations show that anthropogenic emissions contribute up to 30% of the HCHO concentration in the IGP region, with a maximum contributed during the post-monsoon season, which coincides with the lower isoprene concentration (i.e., biogenic emissions) and temperature (Fig. 14). Moreover, Kumar and Sinha (2021) reported high acetaldehyde concentrations from anthropogenic emissions in the IGP region throughout the year. Consequently, anthropogenic emissions are likely to be a significant driver of HCHO concentrations in the IGP region after biogenic emissions.

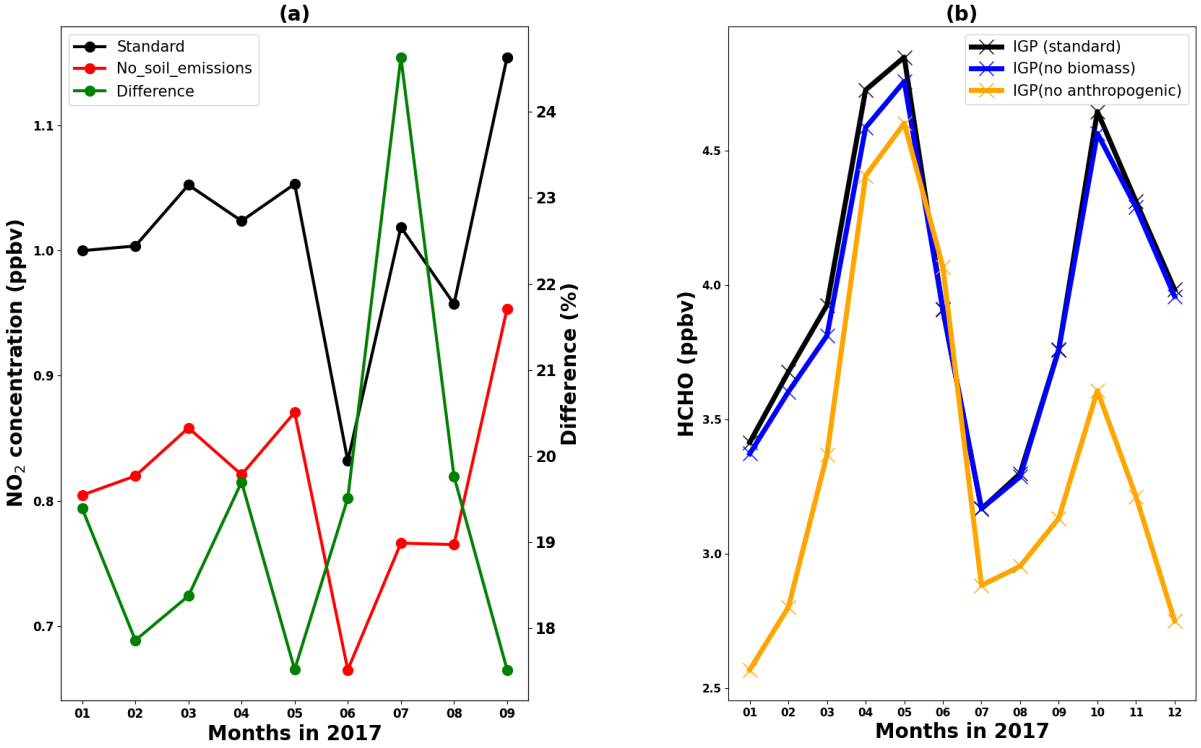

Figure 16. (a)Monthly mean NO_2 concentrations at Phimai were estimated from the standard (black) and L1_NO_2 (red) simulations. The soil NO_x emissions are switched off in the LI_NO_2 simulation. The green line represents the percentage difference between the two simulations. (b) Seasonal variations in the HCHO concentrations in the IGP region, obtained from the standard, L1_HCHO (pyrogenic VOC emission switched off), and L2 simulations

(anthropogenic VOC emissions switched off). The simulations for 2017 are shown and analysed. Daytime values from 09:00-12:00 and 09:00 – 15:00 LT were selected respectively, for Phimai and IGP.

4 Conclusions

Using the JM2 algorithm, NO_2 and HCHO concentrations and profiles were retrieved from MAX-DOAS observations at three A-SKY sites during January 2017 - December 2018. The retrieved products were used to evaluate the global chemistry transport model CHASER simulations at the three sites. At all three locations, the seasonal variation of both trace gases was consistent throughout the investigated period. At Phimai and Pantnagar, biomass burning led to enhanced HCHO and NO_2 concentrations, respectively, during the dry season and spring and post-monsoon season. At Chiba, the HCHO variation was consistent with the temperature-led seasonal changes in biogenic emissions. The changes in the dry season HCHO and NO_2 levels at Phimai during 2015 - 2018 were consistent with the number of fire events.

The R_{FN} values were biased towards a particular regime when the standard transition range $1 < R_{FN} < 2$ was used. The parameterization of Souri et al. (2020) provides a better estimate of the transition region. The classification results of the revised transition region at Phimai and Pantnagar contradicted the results based on the standard transition range. However, they were more reasonable. Such a method based on observations, is therefore influenced by measurement constraints. More observational evidence must be accumulated to standardize this method. Overall, the results clarified that the standard transition region is not valid globally.

Despite the use of an old NO_x emission inventory the simulated NO_2 and HCHO spatial distributions agreed well with those observed from satellite- observations. The modeled regional NO_2 columns estimates were within the 2-sigma variability range of OMI NO_2 retrievals. Although the negative bias in HCHO comparison was higher than that of NO_2, the model demonstrated good capabilities for simulating the HCHO seasonal variation in different regions.

CHASER showed good capabilities at Phimai, characterized as a VOC-rich and low NO_2 (<1 ppbv) region. In both seasons, the observed and modeled profiles (HCHO and NO_2) agreed within the one sigma

standard deviation of the measurements, despite general overestimation of the model. Furthermore, both wet season HCHO profiles were almost identical in the 0.5 – 4 km layer in both datasets.

CHASER demonstrated limited performances at Chiba.NO_2 at higher resolution (i.e.,1.4˚) mainly improved the surface estimates, reducing the overall MBE in the 0 - 2 km layer by 35%. Finer resolution would improve the HCHO estimates in Chiba by 10%; however, it has yet to be underestimated. Sensitivity studies for the Phimai site estimated biomass burning contributions to the respective HCHO and NO_2 concentrations up to ~50 and ~ 35%, respectively. On average, 20% of the NO_2 level originates from soil NO_x emissions, which increased to 25% in July. Anthropogenic emissions (contribution up to 30%) have a more strongly affect VOC variation in the IGP region than biomass burning, which is consistent with reports presented in the literature.

Code availability. The CHASER and JM2 source codes are not available publicly. Dr. Kengo Sudo (kengo@nagoya-u.jp) is the contact person for readers and researchers interested in the CHASER model. In addition, Dr. Hitoshi Irie (hitoshi.irie@chiba-u.jp) will answer queries related to the JM2 codes.

Data availability: The MAX-DOAS data used in the study are publicly accessible on the A-SKY network website (http://atmos3.cr.chiba-u.jp/a-sky/data.html). Upon request, the corresponding author can provide the CHASER simulations and MAX-DOAS averaging kernel data.

Author contributions: HMSH conceptualized the study, conducted the model simulations, analysed the observational and simulation data, and drafted the manuscript. AMF helped with the data processing. HI developed the JM2 code and maintained the A-SKY network. KS developed the CHASER model and supervised the study. MN is the PI of the Pantnagar site. AD and MN shared their experience to explain the results. HI, KS, AD, MN, and AMF commented and provided feedback on the final results and manuscript.

Conflict of Interest: The authors declare that they have no conflict of Interest

Acknowledgments: This research is supported by the Global Environmental Research fund (S-12 and S-20) of the Ministry of the Environment (MOE), Japan, and JSPS KAKENHI Grants: JP20H04320, JP19HO5669, and JP19H04235. The CHASER model simulations are partly performed with the supercomputer (NEC SX-Aurora TSUBASA) at the National Institute for environmental studies (NIES), Tsukuba, Japan.

References

Amnuaylojaroen, T., Inkom, J., Janta, R., & Surapipith, V. : Long range transport of southeast asian pm2. 5 pollution to northern Thailand during high biomass burning episodes. Sustainability, 12(23), 10049. doi: https://doi.org/10.3390/su122310049, 2020

Arlander, D., Brüning, D., Schmidt, U., and Ehhalt, D. : The tropospheric distribution of formaldehyde during TROPOZ II, J. Atmos. Chem., 22(3), 251-269, https://doi.org/10.1007/BF00696637, 1995

Bauwens, M, Verreyken, B, Stavrakou, T, Müller, JF, & De Smedt, I. : Spaceborne evidence for significant anthropogenic VOC trends in Asian cities over 2005–2019. *Environ. Res. Lett.*, *17*(1), 015008. doi:https://iopscience.iop.org/article/10.1088/1748-9326/ac46eb/, 2022

Biswas, M. S., Ghude, S. D., Gurnale, D., Prabhakaran, T., and Mahajan, A. S. : Simultaneous Observations of Nitrogen Dioxide, Formaldehyde and Ozone in the Indo-Gangetic Plain. Aerosol Air Qual. Res., 19(8), 1749-1764, https://doi.org/10.4209/aaqr.2018.12.0484, 2019

Biswas, M. S., & Mahajan, A. S. : Year-long Concurrent MAX-DOAS Observations of Nitrogen Dioxide and Formaldehyde at Pune: Understanding Diurnal and Seasonal Variation Drivers. Aerosol Air Qual. Res., 21(6), 200524. doi:https://doi.org/10.4209/aaqr.200524 ,2021

Boeke, N. L., Marshall, J. D., Alvarez, S., Chance, K. V., Fried, A., Kurosu, T. P., Rappengluck, B., Richter, D.,Walega, J., & Weibring, P. : Formaldehyde columns from the Ozone Monitoring Instrument: Urban versus background levels and evaluation using aircraft data and a global model. J.Geophys.Res, 116(D5). 2011

Bond, D. W., Zhang, R., Tie, X., Brasseur, G., Huffines, G., Orville, R. E., and Boccippio, D. J. : NO_x production by lightning over the continental United States, J. Geophys. Res., 106(D21), 27701-27710, https://doi.org/10.1029/2000JD000191, 2001

Bogumil, K., J. Orphal, T. Homann, S. Voigt, P. Spietz, O. Fleischmann, A. Vogel, M. Hartmann, H. Kromminga, and H. Bovensmann : Measurements of molecular absorption spectra with the SCIAMACHY pre-flight model: instrument characterization and reference data for atmospheric remote-sensing in the 230–2380 nm region, J. Photocho. Photobio. A, 157(2), 167-184, doi:10.1016/S1010-6030(03)00062-5, 2003

Burkert, J., Andrés-Hernández, M. D., Stöbener, D., Burrows, J. P., Weissenmayer, M., & Kraus, A. (2001) : Peroxy radical and related trace gas measurements in the boundary layer above the Atlantic Ocean, J. Geophys. Res., 106(D6), 5457-5477, https://doi.org/10.1029/2000JD900613, 2001

Cárdenas, L., Rondón, A., Johansson, C., & Sanhueza, E. : Effects of soil moisture, temperature, and inorganic nitrogen on nitric oxide emissions from acidic tropical savannah soils. J. Geophys. Res., 98(D8), 14783-14790, https://doi.org/10.1029/93JD01020, 1993

Chaliyakunnel, S., Millet, D. B., and Chen, X. : Constraining emissions of volatile organic compounds over the Indian subcontinent using space-based formaldehyde measurements. J. Geophys. Res., 124(19), 10525-10545, https://doi.org/10.1029/2019JD031262, 2019

Chance, K. V., and R. J. D. Spurr. : Ring effect studies: Rayleigh scattering, including molecular parameters for rotational Raman scattering: and the Fraunhofer spectrum, *Appl. Opt.* , *36*(21), 5224-5230 doi:10.1364/AO.36.005224,1997

Chutia, L., Ojha, N., Girach, I. A., Sahu, L. K., Alvarado, L. M. A., Burrows, J. P., Pathak., P., & Bhuyan, P. K. : Distribution of volatile organic compounds over Indian subcontinent during winter: WRF-chem simulation versus observations. Environ. Pollut., 252, 256-269. doi:https://doi.org/10.1016/j.envpol.2019.05.097, 2019

Clémer, K., Van Roozendael, M., Fayt, C., Hendrick, F., Hermans, C., Pinardi, G., Spurr, R., Wang, P., and De Mazière, M. : Multiple wavelength retrieval of tropospheric aerosol optical properties from MAXDOAS measurements in Beijing, Atmos. Meas. Tech., 3(4), 863-878, https://doi.org/10.5194/amt-3-863-2010, 2010

Colella, P., & Woodward, P. R. : The piecewise parabolic method (PPM) for gas-dynamical simulations. J. Comput. Phys., 54(1), 174-201, https://doi.org/10.1016/0021-9991(84)90143-8, 1984

Crutzen, P. J. : The influence of nitrogen oxides on the atmospheric ozone content. Q. J. Roy. Meteor. Soc., 96(408), 320-325, https://doi.org/10.1002/qj.49709640815, 1970

Davidson, E. A., Vitousek, P. M., Matson, P. A., Riley, R., García-Méndez, G., & Maass, J. M. : Soil emissions of nitric oxide in a seasonally dry tropical forest of Mexico. *J. Geophys. Res., 96*(D8), 15439-15445, https://doi.org/10.1029/91JD01476, 1991

De Smedt, I. , Pinardi, G., Vigouroux, C., Compernolle, S., Bais, A., Benavent, N., Eichmann, K-U., Hedelt, P., Hendricks, F., Irie, H., Kumar, V., Lambert, J-C., Langerock, B., Lerot, C., Liu, C., Loyola, D., Piters, A., Ricjter, A., Cardens, C.R., Romahn, F., Ryan, R.G., Sinha, V., Theys, N., Vlietinck, J., Wagger, T., Wang, T.,YU, H., and Van Roozendael, M.,: Comparative assessment of TROPOMI and OMI formaldehyde observations and validation against MAX-DOAS network column measurements. *Atmos. Chem. Phys., 21*(16), 12561-12593. doi:https://doi.org/10.5194/acp-21-12561-2021, 2021

Duncan, B. N., Yoshida, Y., Damon, M. R., Douglass, A. R., and Witte, J. C. : Temperature dependence of factors controlling isoprene emissions. Geophys. Res. Lett., 36(5), https://doi.org/10.1029/2008GL037090, 2009

Emori, S., Nozawa, T., Numaguti, A., & Uno, I. : Importance of cumulus parameterization for precipitation simulation over East Asia in June. J. Meteorol. Soc. Jpn., 79(4), 939-947. https://doi.org/10.2151/jmsj.79.939, 2001

Fleischmann, O. C., M. Hartmann, J. P. Burrows, and J. Orphal : New ultraviolet absorption cross-sections of BrO at atmospheric temperatures measured by time-windowing Fourier transform spectroscopy, *J. Photocho. Photobio. A, 168*(1), 117-132, doi:10.1016/j.jphotochem.2004.03.026, 2004

Franco, B., Hendrick, F., Van Roozendael, M., Müller, J.-F., Stavrakou, T., Marais, E. A., Bovy, B., Bader, W., Fayt, C., Hermans, C., Lejuene, B., Pinardi, G., Sevais, C., and Mahieu, E. : Retrievals of formaldehyde from ground-based FTIR and MAX-DOAS observations at the Jungfraujoch station and comparisons with GEOS-Chem and IMAGES model simulations. Atmos. Meas. Tech., 8(4), 1733-1756, https://doi.org/10.5194/amt-8-1733-2015, 2015

Fu, T. M., Jacob, D. J., Wittrock, F., Burrows, J. P., Vrekoussis, M., and Henze, D. K. : Global budgets of atmospheric glyoxal and methylglyoxal, and implications for formation of secondary organic aerosols, J. Geophys. Res., 113(D15), https://doi.org/10.1029/2007JD009505, 2008

Frieß, U., Monks, P. S., Remedios, J. J., Rozanov, A., Sinreich, R., Wagner, T., & Platt, U. : MAX-DOAS O4 measurements: A new technique to derive information on atmospheric aerosols: 2. Modeling studies. J. Geophys. Res., 111(D14), https://doi.org/10.1029/2005JD006618, 2006

Frieß, U., Klein Baltink, H., Beirle, S., Clémer, K., Hendrick, F., Henzing, B., Irie, H., de Leeuw, G., Li, A., Moerman, M. M., van Roozendael, M., Shaiganfar, R., Wagner, T., Wang, Y., Xie, P., Yilmaz, S., and Zieger, P. : Intercomparison of aerosol extinction profiles retrieved from MAX-DOAS measurements. Atmos. Meas.Tech., 9(7), 3205-3222, https://doi.org/10.5194/amt-9-3205-2016, 2016

Fukushima, A., Kanamori, H., & Matsumoto, J. : Regionality of long-term trends and interannual variation of seasonal precipitation over India. Prog Earth Planet Sci, 6(1), 1-20. doi:https://doi.org/10.1186/s40645-019-0255-4, 2019

Hak, C., Pundt, I., Trick, S., Kern, C., Platt, U., Dommen, J., Ordóñez, C., Prévôt, A. S. H., Junkermann, W., Astorga-Lloréns, C., Larsen, B. R., Mellqvist, J., Strandberg, A., Yu, Y., Galle, B., Kleffmann, J., Lörzer, J. C., Braathen, G. O., and Volkamer, R. : Intercomparison of four different in-situ techniques for ambient formaldehyde measurements in urban air, *Atmos. Chem. Phys.*, *5*(11), 2881-2900. https://doi.org/10.5194/acp-5-2881-2005, 2005

Hall, S. J., Matson, P. A., and Roth, P. M. : NO_x emissions from soil: implications for air quality modeling in agricultural regions. Annu. Rev. Energy Environ., 21(1), 311-346. https://doi.org/10.1146/annurev.energy.21.1.311, 1996

Halla, J. D., Wagner, T., Beirle, S., Brook, J. R., Hayden, K. L., O'Brien, J. M., Ng, A., Majonis, D., Wenig, M. O., and McLaren, R : Determination of tropospheric vertical columns of NO 2 and aerosol optical properties in a rural setting using MAX-DOAS. Atmos. Chem. Phys., 11(23), 12475-12498, https://doi.org/10.5194/acp-11-12475-2011, 2011

Hendrick, F., Müller, J.-F., Clémer, K., Wang, P., De Mazière, M., Fayt, C., Gielen, C., Hermans, C., Ma, J. Z., Pinardi, G., Stavrakou, T., Vlemmix, T., and Van Roozendael, M.: Four years of ground-based MAX-DOAS observations of HONO and NO_2 in the Beijing area, Atmos. Chem. Phys., 14(2), 765-781, https://doi.org/10.5194/acp-14-765-2014, 2014

Hermans, C., A. Vandaele, S. Fally, M. Carleer, R. Colin, B. Coquart, A. Jenouvrier, and M.-F. Merienne. : Absorption cross-section of the collision-induced bands of oxygen from the UV to the NIR, in Weakly interacting molecular pairs: unconventional absorbers of radiation in the atmosphere, edited, pp. 193-202, Springer,2003.

Hönninger, G., Friedeburg, C. v., and Platt, U. : Multi axis differential optical absorption spectroscopy (MAX-DOAS), Atmos. Chem. Phys., 4(1), 231-254, https://doi.org/10.5194/acp-4-231-2004, 2004

Hoque, H.M. S., Irie, H., and Damiani, A. (2018). First MAX-DOAS Observations of Formaldehyde and Glyoxal in Phimai, Thailand. J. Geophys. Res., 123(17), 9957-9975, https://doi.org/10.1029/2018JD028480, 2018a

Hoque, H. M. S., Irie, H., Damiani, A., Rawat, P., and Naja, M. : First simultaneous observations of formaldehyde and glyoxal by MAX-DOAS in the Indo-Gangetic Plain region. *Sola*. , https://doi.org/10.2151/sola.2018-028, 2018b

Houweling, S., Dentener, F., and Lelieveld, J. : The impact of nonmethane hydrocarbon compounds on tropospheric photochemistry. J. Geophys. Res., 103(D9), 10673-10696, https://doi.org/10.1029/97JD03582, 1998

Huber, D. E., Steiner, A. L., & Kort, E. A. : Daily Cropland Soil NO_x Emissions Identified by TROPOMI and SMAP. Geophys. Res. Lett., 47(22), e2020GL089949, https://doi.org/10.1029/2020GL089949, 2020

Irie, H., Kanaya, Y., Akimoto, H., Iwabuchi, H., Shimizu, A., & Aoki, K. : First retrieval of tropospheric aerosol profiles using MAX-DOAS and comparison with lidar and sky radiometer measurements. Atmos. Chem. Phys., 8(2), 341-350, https://doi.org/10.5194/acp-8-341-2008, 2008a

Irie, H., Kanaya, Y., Akimoto, H., Tanimoto, H., Wang, Z., Gleason, J. F., & Bucsela, E. J. : Validation of OMI tropospheric NO_2 column data using MAX-DOAS measurements deep inside the North China Plain in June 2006: Mount Tai Experiment 2006. Atmos. Chem. Phys., 8(22), 6577-6586,https://doi.org/10.5194/acp-8-6577-2008, 2008b.

Irie, H., Kanaya, Y., Akimoto, H., Iwabuchi, H., Shimizu, A., & Aoki, K. : Dual-wavelength aerosol vertical profile measurements by MAX-DOAS at Tsukuba, Japan. *Atmos. Chem. Phys.*, *9*(8), 2741-2749, https://doi.org/10.5194/acp-9-2741-2009, 2009

Irie, H., Takashima, H., Kanaya, Y., Boersma, K., Gast, L., Wittrock, F., Brunner, D., Zhou, Y., Roozendael, M. V. : Eight-component retrievals from ground-based MAX-DOAS observations. Atmos. Meas. Tech., 4(6), 1027-1044, https://doi.org/10.5194/amt-4-1027-2011, 2011

Irie, H., Nakayama, T., Shimizu, A., Yamazaki, A., Nagai, T., Uchiyama, A., Zaizen, Y., Kagamitani, S., and Matsumi, Y. : Evaluation of MAX-DOAS aerosol retrievals by coincident observations using CRDS, lidar, and sky radiometer inTsukuba, Japan. Atmos. Meas.Tech., 8(7), 2775-2788, https://doi.org/10.5194/amt-8-2775-2015, 2015

Irie, H., Muto, T., Itahashi, S., Kurokawa, J., & Uno, I. : Turnaround of tropospheric nitrogen dioxide pollution trends in China, Japan, and South Korea. *Sola, 12*, 170-174. doi: https://doi.org/10.2151/sola.2016-035, 2016

Irie, H., Yonekawa, D., Damiani, A., Hoque, H.M.S, Sudo, K., & Itahashi, S.; Continuous multi-component MAX-DOAS observations for the planetary boundary layer ozone variation analysis at Chiba and Tsukuba, Japan, from 2013 to 2019. *Prog Earth Planet Sci, 8*(1), 1-11. doi:https://doi.org/10.1186/s40645-021-00424-9,2021

Ito, A., and Inatomi, M. : Use of a process-based model for assessing the methane budgets of global terrestrial ecosystems and evaluation of uncertainty. Biogeosciences, 9(2), 759-773. https://doi.org/10.5194/bg-9-759-2012, 2012

Iwabuchi, H. :Efficient Monte Carlo methods for radiative transfer modeling. J. Atmos. Sci., 63(9), 2324-2339, https://doi.org/10.1175/JAS3755.1, 2006

Jang, M., and Kamens, R. M. : Characterization of secondary aerosol from the photooxidation of toluene in the presence of NO_x and 1-propene, Environ. Sci. Technol., 35(18), 3626-3639. https://doi.org/10.1021/es010676+, 2001

Jin, X., Fiore, A. M., Murray, L. T., Valin, L. C., Lamsal, L. N., Duncan, B., Boersma, K.F., De Smedt, I., Abad, G.G., Chance, K., and Tonnesen, G. : Evaluating a space-based indicator of surface ozone-NOx-VOC

sensitivity over midlatitude source regions and application to decadal trends. J. Geophys. Res., 122(19), 10,439-410,461, https://doi.org/10.1002/2017JD026720, 2017

Jin, X., & Holloway, T. (2015). Spatial and temporal variability of ozone sensitivity over China observed from the Ozone Monitoring Instrument. J. Geophys.Res., 120(14), 7229-7246. doi: https://doi.org/10.1002/2015JD023250

Jenkin, M.E., Young, J.C., & Rickard, A.R. : The MCM v3. 3.1 degradation scheme for isoprene. Atmos. Chem. Phys., 15(20), 11433-11459. doi:https://doi.org/10.5194/acp-15-11433-2015, 2015

K-1 model developers : K-1 Coupled GCM (MIROC) description, Tech .rep., Center for Climate System Research (University of Tokyo), National Institute for Environemntal Studies, and Frontier Research Center for Global Change, available at : http://ccsr.aori.u-tokyo.ac.jp/~hasumi/miroc_description.pdf, 2004

Kanakidou, M., Seinfeld, J. H., Pandis, S. N., Barnes, I., Dentener, F. J., Facchini, M. C., Van Dingenen, R., Ervens, B., Nenes, A., Nielsen, C. J., Swietlicki, E., Putaud, J. P., Balkanski, Y., Fuzzi, S., Horth, J., Moortgat, G. K., Winterhalter, R., Myhre, C. E. L., Tsigaridis, K., Vignati, E., Stephanou, E. G., and Wilson, J. : Organic aerosol and global climate modelling: a review. Atmos. Chem. Phys., 5(4), 1053-1123, https://doi.org/10.5194/acp-5-1053-2005

Kanaya, Y., Irie, H., Takashima, H., Iwabuchi, H., Akimoto, H., Sudo, K., Gu, M., Chong, J., Kim, Y. J., Lee, H., Li, A., Si, F., Xu, J., Xie, P.-H., Liu, W.-Q., Dzhola, A., Postylyakov, O., Ivanov, V., Grechko, E., Terpugova, S., and Panchenko, M.: Long-term MAX-DOAS network observations of NO₂ in Russia and Asia (MADRAS) during the period 2007–2012: instrumentation, elucidation of climatology, and comparisons with OMI satellite observations and global model simulations. Atmos. Chem. Phys., 14(15), 7909-7927, https://doi.org/10.5194/acp-14-7909-2014, 2014

Kannari, A., Tonooka, Y., Baba, T., & Murano, K. : Development of multiple-species 1km× 1km resolution hourly basis emissions inventory for Japan. Atmos. Environ., 41(16), 3428-3439. doi:https://doi.org/10.1016/j.atmosenv.2006.12.015, 2007

Khodmanee, S., & Amnuaylojaroen, T., Impact of Biomass Burning on Ozone, Carbon Monoxide, and Nitrogen Dioxide in Northern Thailand. *Front. Enviorn. Sci., 9*, 27. doi:https://doi.org/10.3389/fenvs.2021.641877, 2021

Kreher, K., Van Roozendael, M., Hendrick, F., Apituley, A., Dimitropoulou, E., Frieß, U., Richter, A., Wagner, T., Lampel, J., Abuhassan, N., Ang, L., Anguas, M., Bais, A., Benavent, N., Bösch, T., Bognar, K., Borovski, A., Bruchkouski, I., Cede, A., Chan, K. L., Donner, S., Drosoglou, T., Fayt, C., Finkenzeller, H., Garcia-Nieto, D., Gielen, C., Gómez-Martín, L., Hao, N., Henzing, B., Herman, J. R., Hermans, C., Hoque, S., Irie, H., Jin, J., Johnston, P., Khayyam Butt, J., Khokhar, F., Koenig, T. K., Kuhn, J., Kumar, V., Liu, C., Ma, J., Merlaud, A., Mishra, A. K., Müller, M., Navarro-Comas, M., Ostendorf, M., Pazmino, A., Peters, E., Pinardi, G., Pinharanda, M., Piters, A., Platt, U., Postylyakov, O., Prados-Roman, C., Puentedura, O., Querel, R., Saiz-Lopez, A., Schönhardt, A., Schreier, S. F., Seyler, A., Sinha, V., Spinei, E., Strong, K., Tack, F., Tian, X., Tiefengraber, M., Tirpitz, J.-L., van Gent, J., Volkamer, R., Vrekoussis, M., Wang, S., Wang, Z., Wenig, M., Wittrock, F., Xie, P. H., Xu, J., Yela, M., Zhang, C., and Zhao, X.: Intercomparison of NO_2, O_4, O_3 and HCHO slant column measurements by MAX-DOAS and zenith-sky UV–visible spectrometers during CINDI-2. Atmos. Meas. Tech., 13(5), 2169-2208, https://doi.org/10.5194/amt-13-2169-2020, 2020

Kumar, V., Beirle, S., Dörner, S., Mishra, A. K., Donner, S., Wang, Y., Sinha,V., and Wagner, T. (2020). Long-term MAX-DOAS measurements of NO2, HCHO, and aerosols and evaluation of corresponding satellite data products over Mohali in the Indo-Gangetic Plain. Atmos. Chem. Phys., *20*(22), 14183-14235. doi:10.5194/acp-20-14183-2020

Kumar, V., & Sinha, V. (2021), Season-wise analyses of VOCs, hydroxyl radicals and ozone formation chemistry over north-west India reveal isoprene and acetaldehyde as the most potent ozone precursors throughout the year. Chemosphere, *283*, 131184. doi:https://doi.org/10.1016/j.chemosphere.2021.131184

Kurucz, R. L., Furenlid, I., Brault, J., and Testerman, L. : Solar Flux Atlas from 296 to 1300 nm. Natl. Sol. Obs., Sunspot, New Mexico, 240, 1984

Lee, M., Heikes, B. G., Jacob, D. J., Sachse, G., and Anderson, B. : Hydrogen peroxide, organic hydroperoxide, and formaldehyde as primary pollutants from biomass burning, J. Geophys. Res., 102(D1), 1301-1309, https://doi.org/10.1029/96JD01709, 1997

Lin, S.-J., & Rood, R. B. : Multidimensional flux-form semi-Lagrangian transport schemes. Mon. Weather Rev., 124(9), 2046-2070, https://doi.org/10.1175/1520-0493(1996)124<2046:MFFSLT>2.0.CO;2, 1996

Ma, J., Beirle, S., Jin, J., Shaiganfar, R., Yan, P., and Wagner, T. : Tropospheric NO_2 vertical column densities over Beijing: results of the first three years of ground-based MAX-DOAS measurements (2008–2011) and satellite validation,Atmos. Chem. Phys., 13(3), 1547-1567, https://doi.org/10.5194/acp-13-1547-2013, 2013

Mallik, C., & Lal, S. : Seasonal characteristics of SO_2, NO_2, and CO emissions in and around the Indo-Gangetic Plain, Environ Monit Assess, *186*(2), 1295-1310, https://doi.org/10.1007/s10661-013-3458-y,2015

Martin, R. V., Fiore, A. M., and Van Donkelaar, A. : Space-based diagnosis of surface ozone sensitivity to anthropogenic emissions, Geophys. Res. Lett., 31(6), https://doi.org/10.1029/2004GL019416, 2004

Mahajan, A. S., De Smedt, I., Biswas, M. S., Ghude, S., Fadnavis, S., Roy, C., and van Roozendael, M. : Inter-annual variations in satellite observations of nitrogen dioxide and formaldehyde over India. Atmos. Environ., 116, 194-201, https://doi.org/10.1016/j.atmosenv.2015.06.004, 2015

Meller, R., and G. K. Moortgat. : Temperature dependence of the absorption cross sections of formaldehyde between 223 and 323 K in the wavelength range 225–375 nm, *J. Geophys. Res., 105*(D6), 7089-7101, doi:10.1029/1999JD901074, 2000

Mellor, G. L., & Yamada, T. : A hierarchy of turbulence closure models for planetary boundary layers. J. Atmos. Sci., 31(7), 1791-1806, https://doi.org/10.1175/1520-0469(1974)031<1791:AHOTCM>2.0.CO;2, 1974

Mishra, A. K., and Sinha, V. : Emission drivers and variability of ambient isoprene, formaldehyde and acetaldehyde in north-west India during monsoon season, Environ. Pollut., 267, 115538, https://doi.org/10.1016/j.envpol.2020.115538, 2020

Miyazaki, K., Bowman, K., Sekiya, T., Eskes, H., Boersma, F., Worden, H., Livesey, N., Payne, V.H., Sudo, K., Kanaya, Y., Takigawa, M., and Ogochi, K. (2020). Updated tropospheric chemistry reanalysis and emission estimates, TCR-2, for 2005–2018. Earth Syst. Sci. Data, 12(3), 2223-2259. doi:10.5194/essd-12-2223-2020

Miyazaki, K., Eskes, H., Sudo, K., Boersma, K. F., Bowman, K., and Kanaya, Y. : Decadal changes in global surface NOx emissions from multi-constituent satellite data assimilation. Atmos. Chem. Phys., 17(2), 807-837, https://doi.org/10.5194/acp-17-807-2017, 2017

Morino, Y, Ohara, T, Yokouchi, Y, & Ooki, A. : Comprehensive source apportionment of volatile organic compounds using observational data, two receptor models, and an emission inventory in Tokyo metropolitan area. J. Geophys. Res., 116(D2),doi:https://doi.org/10.1029/2010JD014762, 2011

Nair, V. S., Moorthy, K. K., Alappattu, D. P., Kunhikrishnan, P.K., George, S., Nair, P. R., Babu, S.S., Abish, A., Satheesh, S.K., Tripathi, S. N., Niranjan, K., Madhavan, B.L., Srikant, V., Dutt, C.B.S., Badarinath, K>V>S., & Reddy, R.R.: Wintertime aerosol characteristics over the Indo-Gangetic Plain (IGP): Impacts of local boundary layer processes and long-range transport. J. Geophys. Res., 112(D13). doi:https://doi.org/10.1029/2006JD008099, 2007

Ohara, T., Akimoto, H., Kurokawa, J., Horii, N., Yamaji, K., Yan, X., & Hayasaka, T. : An Asian emission inventory of anthropogenic emission sources for the period 1980–2020. Atmos. Chem. Phys., 7(16), 4419-4444. doi:https://doi.org/10.5194/acp-7-4419-2007, 2007

Platt, U. : Differential optical absorption spectroscopy (DOAS), in Chemical Analysis Series, edited, pp. 27-84, Wiley & Sons. Inc., 1994

Platt, U., and Stutz, J. : Differential Optical Absorption Spectroscopy, Springer, 2008

Price, C., & Rind, D. : A simple lightning parameterization for calculating global lightning distributions. *J. Geophys. Res.*, *97*(D9), 9919-9933, https://doi.org/10.1029/92JD00719, 1992

Rodgers, C. D. : Inverse methods for atmospheric sounding: theory and practice, World scientific Singapore, 2008

Roscoe, H. K., Van Roozendael, M., Fayt, C., du Piesanie, A., Abuhassan, N., Adams, C., Akrami, M., Cede, A., Chong, J., Clémer, K., Friess, U., Gil Ojeda, M., Goutail, F., Graves, R., Griesfeller, A., Grossmann, K., Hemerijckx, G., Hendrick, F., Herman, J., Hermans, C., Irie, H., Johnston, P. V., Kanaya, Y., Kreher, K.,

Leigh, R., Merlaud, A., Mount, G. H., Navarro, M., Oetjen, H., Pazmino, A., Perez-Camacho, M., Peters, E., Pinardi, G., Puentedura, O., Richter, A., Schönhardt, A., Shaiganfar, R., Spinei, E., Strong, K., Takashima, H., Vlemmix, T., Vrekoussis, M., Wagner, T., Wittrock, F., Yela, M., Yilmaz, S., Boersma, F., Hains, J., Kroon, M., Piters, A., and Kim, Y. J. : Intercomparison of slant column measurements of NO_2 and O_4 by MAX-DOAS and zenith-sky UV and visible spectrometers. Atmos. Meas. Tech., 3(6), 1629-1646, https://doi.org/10.5194/amt-3-1629-2010, 2010

Ryan, R. G., Rhodes, S., Tully, M., & Schofield, R. : Surface ozone exceedances in Melbourne, Australia are shown to be under NO_x control, as demonstrated using formaldehyde: NO_2 and glyoxal: formaldehyde ratios, Sci. Total Environ., 749, 141460, https://doi.org/10.1016/j.scitotenv.2020.141460, 2020

Sadavarte, P., & Venkataraman, C. : Trends in multi-pollutant emissions from a technology-linked inventory for India: I. Industry and transport sectors. Atmos. Environ., 99, 353-364. doi:https://doi.org/10.1016/j.atmosenv.2014.09.081, 2014

Sarmah, S., Singha, M., Wang, J., Dong, J., Burman, P. K. D., Goswami, S., Ge. Y., Ilyas, S., & Niu, S. : Mismatches between vegetation greening and primary productivity trends in South Asia–A satellite evidence. Int. J. Appl. Eath Obs., 104, 102561. doi:https://doi.org/10.1016/j.jag.2021.102561, 2021

Schindlbacher, A., Zechmeister-Boltenstern, S., & Butterbach-Bahl, K. : Effects of soil moisture and temperature on NO, NO_2, and N_2O emissions from European forest soils. J. Geophys. Res., 109(D17), https://doi.org/10.1029/2004JD004590, 2004

Schroeder, J. R., Crawford, J. H., Fried, A., Walega, J., Weinheimer, A., Wisthaler, A., Muller, M., Mikovinu, T., Chen,G., Shook, M. : New insights into the column CH_2O/NO_2 ratio as an indicator of near-surface ozone sensitivity. J.Geophys. Res., 122(16), 8885-8907. doi: https://doi.org/10.1002/2017JD026781,2017

Sharma, S., Goel, A., Gupta, D., Kumar, A., Mishra, A. , Kundu, S., Chatani, S., and Klimont, Z. : Emission inventory of non-methane volatile organic compounds from anthropogenic sources in India. Atmos. Environ., 102, 209-219. doi:https://doi.org/10.1016/j.atmosenv.2014.11.070, 2015

Seco, R., Penuelas, J., and Filella, I. : Short-chain oxygenated VOCs: Emission and uptake by plants and atmospheric sources, sinks, and concentrations, Atmos. Environ., 41(12), 2477-2499, https://doi.org/10.1016/j.atmosenv.2006.11.029, 2007

Sekiya, T., & Sudo, K. : Roles of transport and chemistry processes in global ozone change on interannual and multidecadal time scales. J. Geophys. Res., 119(8), 4903-4921. doi:https://doi.org/10.1002/2013JD020838, 2014

Sekiya, T., Miyazaki, K., Ogochi, K., Sudo, K., & Takigawa, M. : Global high-resolution simulations of tropospheric nitrogen dioxide using CHASER V4.0. *Geosci. Model Dev., 11*(3), 959-988. http://doi.org/10.5194/gmd-11-959-2018, 2018

Seinfeld, J. H., & Pandis, S. N. : Atmospheric chemistry and physics: from air pollution to climate change: John Wiley & Sons, New York, 1998

Sindelarova, K., Markova, J., Simpson, D., Huszar, P., Karlicky, J., Darras, S., & Granier, C. : High-resolution biogenic global emission inventory for the time period 2000–2019 for air quality modelling. *Earth Syst. Sci. Data, 14*(1), 251-270. doi:https://doi.org/10.5194/essd-14-251-2022, 2022

Singh, H., Salas, L., Chatfield, R., Czech, E., Fried, A., Walega, J., Evans, M.J., Field, B.D., Jacob, D.J., Blake, D., Heikes, B., Talbolt, R., Sachse, G., Crawford, J.H., Avery, M.A., Sandholm, S., and Fuelberg, H. : Analysis of the atmospheric distribution, sources, and sinks of oxygenated volatile organic chemicals based on measurements over the Pacific during TRACE-P, J. Geophys. Res., 109(D15), https://doi.org/10.1029/2003JD003883, 2004

Sinreich, R., Frieß, U., Wagner, T., and Platt, U. : Multi axis differential optical absorption spectroscopy (MAX-DOAS) of gas and aerosol distributions, Faraday discuss., 130, 153-164, https://doi.org/10.1039/B419274P, 2005

Solomon, S., Portmann, R., Sanders, R., Daniel, J., Madsen, W., Bartram, B., and Dutton, E. : On the role of nitrogen dioxide in the absorption of solar radiation, J. Geophys. Res., 104(D10), 12047-12058, https://doi.org/10.1029/1999JD900035, 1999

Souri, A. H., Nowlan, C. R., Wolfe, G. M., Lamsal, L. N., Miller, C. E. C., Abad, G. G., Janz, S., Fried, A., Blake, D. R., Weinheimer, A. J. , Diskin, G.S., Liu, X., and Chance, K. : Revisiting the effectiveness of $HCHO/NO_2$ ratios for inferring ozone sensitivity to its precursors using high resolution airborne remote sensing observations in a high ozone episode during the KORUS-AQ campaign. Atmos. Environ., 224, 117341, https://doi.org/10.1016/j.atmosenv.2020.117341, 2020

Sudo, K., & Akimoto, H. (2007). Global source attribution of tropospheric ozone: Long-range transport from various source regions. J. Geeophys. Res., 112(D12), https://doi.org/10.1029/2006JD007992, 2007

Sudo, K., Takahashi, M., Kurokawa, J., & Akimoto, H. : CHASER: A global chemical model of the troposphere 1. Model description. J. Geophys. Res., 107, 4339, https://doi.org/10.1029/2001JD001113, 2002

Surl, L., Palmer, P. I., & González Abad, G. : Which processes drive observed variations of HCHO columns over India? Atmos. Chem. Phys., 18(7), 4549-4566 ,https://doi.org/10.5194/acp-18-4549-2018, 2018

Takemura, T., Nozawa, T., Emori, S., Nakajima, T. Y., & Nakajima, T. : Simulation of climate response to aerosol direct and indirect effects with aerosol transport-radiation model. J. Geophys. Res., 110(D2), https://doi.org/10.1029/2004JD005029, 2005

Takemura, T., Egashira, M., Matsuzawa, K., Ichijo, H., O'ishi, R., & Abe-Ouchi, A. : A simulation of the global distribution and radiative forcing of soil dust aerosols at the Last Glacial Maximum. Atmos. Chem. Phys., 9(9), 3061-3073, https://doi.org/10.5194/acp-9-3061-2009, 2009

Tonnesen, G. S., & Dennis, R. L. (2000). Analysis of radical propagation efficiency to assess ozone sensitivity to hydrocarbons and NO_x: 1. Local indicators of instantaneous odd oxygen production sensitivity. J.Geophys. Res., 105(D7), 9213-9225. doi:https://doi.org/10.1029/1999JD900371

Vandaele, A., C. Hermans, P. Simon, M. Van Roozendael, J. Guilmot, M. Carleer, and R. Colin.: Fourier transform measurement of NO2 absorption cross-section section in the visible range at room temperature, J. Atmos. Chem., 25(3), 289-305, doi:10.1007/BF00053797, 2009

Vandaele, A. C., C. Fayt, F. Hendrick, C. Hermans, F. Humbled, M. V. Roozendael, M. Gil, M. Navarro, O. Puentedura, M. Yela, G. Braathen, K. Stebel, K. Tornkvist, P. Jhonston, K. Kreher, F. Goutail, F. Mieville, J.P. Pommereau, S. Khaikine, A. Richter, H. Oetjen, F. Wittrock, S. Bugarski, U. Friess, K. Pfeilsticker, R. Sinreich, T. Wagner, G. Corlett, and R. Leigh), An intercomparison campaign of ground-based UV-visible measurements of NO_2, BrO, and OClO slant columns Methods of analysis and results for NO_2, J. Geophys Res, 110(D8),2005

Vigouroux, C., Hendrick, F., Stavrakou, T., Dils, B., De Smedt, I., Hermans, C., Merlaud, A., Scolas, F., Senten, C., Vanhaelewyn, G., Fally, S., Carleer, M., Metzger, J.-M., Müller, J.-F., Van Roozendael, M., and De Mazière, M.: Ground-based FTIR and MAX-DOAS observations of formaldehyde at Réunion Island and comparisons with satellite and model data, Atmos. Chem. Phys., 9(24), 9523-9544, https://doi.org/10.5194/acp-9-9523-2009, 2009

Wagner, T., Dix, B. v., Friedeburg, C. v., Frieß, U., Sanghavi, S., Sinreich, R., & Platt, U. : MAX-DOAS O4 measurements: A new technique to derive information on atmospheric aerosols—Principles and information content. J. Geophys. Res., 109(D22). doi: https://doi.org/10.1029/2004JD004904, 2004

Wagner, T., Burrows, J., Deutschmann, T., Dix, B., Friedeburg, C. v., Frieß, U., Iwabuchi, H. , Hendrick, F., Heue, K.-P., Irie, H., Iwabuchi, H., Kanaya, Y., Keller, J., McLinden, C. A., Oetjen, H., Palazzi, E., Petritoli, A., Platt, U., Postylyakov, O., Pukite, J., Richter, A., van Roozendael, M., Rozanov, A., Rozanov, V., Sinreich, R., Sanghavi, S., and Wittrock, F. : Comparison of box-air-mass-factors and radiances for Multiple-Axis Differential Optical Absorption Spectroscopy (MAX-DOAS) geometries calculated from different UV/visible radiative transfer models. Atmos. Chem. Phys., 7(7), 1809-1833. doi:https://doi.org/10.5194/acp-7-1809-2007, 2007

Wang, T., Hendrick, F., Wang, P., Tang, G., Clémer, K., Yu, H., Fayt, C., Hermans, C., Gielen, C., Müller, J.-F., Pinardi, G., Theys, N., Brenot, H., and Van Roozendael, M. : Evaluation of tropospheric SO_2 retrieved from MAX-DOAS measurements in Xianghe, China. Atmos. Chem. Phys., 14(20), 11149-11164, https://doi.org/10.5194/acp-14-11149-2014, 2014

Wesely, M. : Parameterization of surface resistances to gaseous dry deposition in regional-scale numerical models. Atmos. Environ., 41, 52-63. https://doi.org/10.1016/j.atmosenv.2007.10.058, 1989

Williams, J. E., Boersma, K. F., Sager, P. L., & Verstraeten, W. W,. The high-resolution version of TM5-MP for optimized satellite retrievals: description and validation. Geosci. Model Dev., 10(2), 721-750. doi:https://doi.org/10.5194/gmd-10-721-2017,2017

Wittrock, F., Oetjen, H., Richter, A., Fietkau, S., Medeke, T., Rozanov, A., and Burrows, J. : MAX-DOAS measurements of atmospheric trace gases in Ny-Ålesund-Radiative transfer studies and their application, Atmos. Chem. Phys., 4(4), 955-966, https://doi.org/10.5194/acp-4-955-2004, 2004

Woo, J-H., Kim, Y. , Kim, H-K., Choi, K-C., Eum, J-H., Lee, J-B., Lim, J-H., Kim,J., and Seong, M. : Development of the CREATE inventory in support of integrated climate and air quality modeling for Asia. Sustainability, 12(19), 7930. doi:https://doi.org/10.3390/su12197930, 2020